



www.sciencemag.org/cgi/content/full/science.aan5630/DC1

Supplementary Materials for
Dynamic multinuclear sites formed by mobilized copper ions in NO_x selective catalytic reduction

Christopher Paolucci, Ishant Khurana, Atish A. Parekh, Sichi Li, Arthur J. Shih, Hui Li, John R. Di Iorio, Jonatan D. Albarracin-Caballero, Aleksey Yezerets, Jeffrey T. Miller, W. Nicholas Delgass, Fabio H. Ribeiro, William F. Schneider,* Rajamani Gounder*

*Corresponding author. Email: w Schneider@nd.edu (W.F.S.); rgounder@purdue.edu (R.G.)

Published 17 August 2017 on *Science* First Release
DOI: 10.1126/science.aan5630

This PDF file includes:

Materials and Methods
Figs. S1 to S20
Tables S1 to S11
References

Other Supplementary Materials for this manuscript includes the following:
(available at www.sciencemag.org/cgi/content/full/science.aan5630/DC1)

Database S1 CONTCARs (zipped archive)

Materials and Methods

S1. Synthesis Methods and Characterization

Synthesis of SSZ-13 zeolites

Here, SSZ-13 is used to refer to materials of aluminosilicate composition and the chabazite (CHA) framework. High-aluminum SSZ-13 zeolites (Si/Al = 4.5) were synthesized as previously reported (10). A molar ratio of 1 SiO₂/ 0.031 Al₂O₃/ 0.017 TMAdaOH/ 0.770 Na₂O/ 12.1 H₂O was used in the synthesis solution. Briefly, a 1M NaOH solution (3.3 wt% NaOH, Alfa Aesar) was added to deionized water (18.2 MΩ) in a perfluoroalkoxy alkane (PFA) jar and stirred for 15 minutes at ambient conditions. Next, sodium silicate (10.6 wt % Na₂O, 25.6 wt% SiO₂; Sigma Aldrich) was added to the NaOH solution and stirred for 15 minutes under ambient conditions. Then, NH₄-Y zeolite (Zeolyst CBV300, Si/Al = 2.6) was added and the mixture was stirred for 30 minutes under ambient conditions. Finally, an aqueous TMAdaOH solution (25 wt%, Sachem) was added to the mixture and stirred for 30 minutes under ambient conditions. The synthesis mixture was then transferred to 45 mL Teflon-lined stainless steel autoclaves (Parr Instruments) and placed in a forced convection oven (Yamato DKN-402C) at 413 K and rotated at 60 RPM for 6 days.

Low aluminum SSZ-13 zeolites (Si/Al = 15-25) were synthesized in hydroxide media using a previously reported procedure (10). A molar ratio of 1 SiO₂/ 0.0167-0.033 Al₂O₃/ 0.25 TMAdaOH/ 0.125 Na₂O/ 44 H₂O was used to obtain Na⁺/TMAda⁺ = 1 and Si/Al = 15 or 25 in the synthesis solution. A typical synthesis involved adding an aqueous TMAdaOH solution to deionized H₂O in a PFA jar and stirring the solution under ambient conditions for 15 minutes. Next, aluminum hydroxide was added to the aqueous TMAdaOH solution. Then, a 5M NaOH solution (16.7 wt% NaOH in deionized water; NaOH pellets 98 wt%, Alfa Aesar) was added dropwise to the solution and stirred under ambient conditions for 15 minutes. Finally, colloidal silica was added and the mixture was stirred for 2 h under ambient conditions. All synthesis reagents were used without further purification. The synthesis solution was then transferred to a 45 mL Teflon-lined stainless steel autoclave and placed in a forced convection oven at 433 K and rotated at 40 RPM for 6 days.

X-Ray diffraction of CHA zeolites

The CHA crystal framework was determined from powder X-ray diffraction (XRD) patterns measured on a Rigaku SmartLab X-ray diffractometer with a Cu Kα radiation source (λ=0.154 nm) operated at 1.76 kW. 0.01 g of zeolite powder were loaded onto a low-volume sample holder (Rigaku) and the diffraction pattern was recorded from 4-40° 2θ at a scan rate of 0.04° s⁻¹. Powder XRD patterns for all synthesized materials were compared to diffraction patterns for CHA reported in the International Zeolite Association (IZA) structure database (36). All XRD patterns reported here are normalized such that the maximum peak intensity in each pattern is unity. Diffraction patterns of CHA zeolites are shown in Fig. S1.

Adsorption isotherms to measure micropore volumes of CHA zeolites

Micropore volumes of CHA zeolites were determined from Ar adsorption isotherms measured at 87 K on a Micromeritics ASAP 2020 Surface Area and Porosity Analyzer. Typically, 0.03–0.05 g of pelleted and sieved sample (nominal diameter between 180–250 μm) were degassed by heating to 393 K (0.167 K s^{-1}) under vacuum ($<5 \mu\text{mHg}$) for 2 h, and then further heating to 623 K (0.167 K s^{-1}) under vacuum ($<5 \mu\text{mHg}$) and holding for 9 h. Volumetric gas adsorption within micropores ($\text{cm}^3 \text{ g}^{-1}$ at STP) was estimated from analysis of semi-log derivative plots of the adsorption isotherm ($\partial(V_{\text{ads}})/\partial(\ln(P/P_0))$ vs. $\ln(P/P_0)$) to identify the micropore filling transition (first maximum) and then the end of micropore filling (subsequent minimum). Micropore volumes ($\text{cm}^3 \text{ g}^{-1}$) were obtained on SSZ-13 zeolites by converting standard gas adsorption volumes ($\text{cm}^3 \text{ g}_{\text{cat}}^{-1}$ at STP) to liquid volumes using a density conversion factor assuming the liquid density of Ar at 87 K. Micropore volumes of CHA zeolites are shown in Fig. S2. In each figure, adsorption isotherms are offset in increments of $200 \text{ cm}^3 \text{ g}^{-1}$ for clarity.

Aqueous-phase Copper Ion-Exchange of H-SSZ-13

Cu-SSZ-13 zeolites were prepared by aqueous-phase Cu ion-exchange using $\text{Cu}(\text{NO}_3)_2$ as the precursor. A pH meter (Mettler Toledo SevenEasy™ pH Meter S20) calibrated at pH values of 1.0 (Sigma Aldrich FLUKA 31044 Buffer solution pH 1.0 at 20°C), 4.0 (Hach Buffer Solution pH 4.0 ± 0.02 at 25°C), and 7.0 (Hach Buffer Solution pH 7.00 ± 0.02 at 25°C) was used to monitor the pH throughout the Cu ion-exchange process.

Typically, 1 to 2 g of H-SSZ-13 were added to 40 mL of deionized water (Millipore, Synergy UV Water Purification System, $18.2 \text{ M}\Omega \text{ cm}^{-1}$ resistivity at 298 K) in a 250 mL borosilicate Erlenmeyer flask and stirred at 300 rpm using a magnetic stir bar for 30 minutes at 313 K. Depending on the Cu exchange level targeted, 20 to 100 mL of 0.001 M to 0.1M $\text{Cu}(\text{NO}_3)_2$ solution (Sigma Aldrich, Copper^{II} nitrate hydrate, 99.999% trace metals basis) was added to the slurry. The pH was controlled to 4.9 ± 0.1 by dropwise addition (~ 2 drops per second) of 1.0 M NH_4OH (Sigma Aldrich, 28.0% Ammonium hydroxide solution, ACS reagent grade) immediately after addition of $\text{Cu}(\text{NO}_3)_2$ and was maintained at 4.9 ± 0.1 for 4 hours. Cu-exchanged SSZ-13 was recovered via centrifugation, and then washed with deionized water six times ($70 \text{ mL H}_2\text{O g}_{\text{catalyst}}^{-1}$ per wash). Cu-SSZ-13 catalysts were dried at 373 K in ambient air in a free convection oven for 12 hours, crushed with a mortar and pestle, then treated in flowing dry air ($100 \text{ mL g}_{\text{catalyst}}^{-1}$, Indiana Oxygen, Zero grade air, $< 1 \text{ ppm THC}$) to 773 K at a rate of 1 K min^{-1} .

Elemental Analysis using Atomic Absorption Spectroscopy

Typically, 0.02–0.050 g of dry sample (H-SSZ-13 or Cu-SSZ-13) were dissolved in approximately 2 mL of hydrofluoric acid (HF) (Mallinckrodt Baker, 48% HF, Baker Analyzed® A.C.S. Reagent) in a 60 mL high density polyethylene (HDPE) bottle (2 oz.,

60 mL Nalgene™ Wide-Mouth Amber HDPE bottles). A polyethylene pipet was used to transfer the HF. The sample was capped and left to dissolve for 12 hours then diluted with approximately 50 mL of deionized water (Millipore, Synergy UV Water Purification System, 18.2 MΩ cm⁻¹ resistivity at 298 K).

Bulk elemental composition was determined using atomic absorption spectroscopy (AAS) on a Perkin Elmer AAnalyst 300. Silicon AAS standards were created by diluting a 1000 ppm silicon AAS standard solution (Sigma Aldrich, TraceCERT®, 1000 mg/L Si in NaOH) to 15, 75, and 150 ppm. A linear calibration curve (ppm_{Si} versus Si absorbance at 251.6 nm) was determined by plotting the absorbance of each silicon standard at 251.6 nm. Similar procedures were used for aluminum, copper and sodium on all reported SSZ-13 catalysts.

Cu site characterization and quantification

Cu K-edge X-ray absorption near edge spectroscopy (XANES) of samples under ambient conditions were indistinguishable from that of an aqueous Cu^{II} nitrate solution (Cu-CHA-20 and Cu-CHA-29 shown in Fig. S3) and did not show absorption characteristic of Cu^I (edge at ~8983 eV (37, 38)) or of Cu^{II} within Cu_xO_y clusters (39, 40). Diffuse reflectance UV-Visible spectra collected on these samples under ambient, hydrated conditions are shown in Fig. S4. The peak at 12500 cm⁻¹ is representative of hydrated isolated Cu^{II} ions. Peaks at ~22500 cm⁻¹, reported to be due to Cu-dimers in ZSM-5 (41), are not observed, indicating that predominantly isolated Cu^{II} species are present. The broad absorption features between 30000 cm⁻¹ and 50000 cm⁻¹ are due to contributions from the zeolite framework.

The enumeration of isolated Cu^{II} and Cu^{II}OH sites on each Cu-CHA zeolite was determined after oxidative treatment (20% O₂, 773 K) by quantifying the number of residual protons that remained after Cu exchange, given that Cu^{II} sites exchange two protons and Cu^{II}OH sites exchange one proton. The quantification was performed using methods that selectively titrate residual H⁺ sites in small-pore, metal-exchanged zeolites (42), in which NH₃-saturated samples are purged in flowing wet helium (3% H₂O in He, 433 K) to desorb Lewis acid-bound NH₃, prior to temperature programmed desorption (Table S1). The Cu^{II} and Cu^{II}OH site quantities in the samples studied here are consistent with the thermodynamic preference for Cu^{II} exchange at paired Al sites until saturation (10), followed by further exchange of Cu^{II}(OH) sites at isolated Al. Taken together, the *ex situ* characterization of Cu sites by X-ray absorption, UV-Visible and quantification of residual H⁺ sites by NH₃ titration, confirm that the Cu-CHA samples studied here contain only isolated Cu^{II} cations, present either as Cu^{II} at paired framework Al sites or as [CuOH]⁺ at isolated Al sites (10).

S2. SCR Kinetics

Standard selective catalytic reduction (SCR) kinetic data were measured on a down-flow 3/8" ID tubular quartz reactor. All samples were pelletized (Specac 13mm Diameter Stainless Steel Evaluable Pellet Die) under 10,000 psi pressure (Carver Laboratory Press), ground using a mortar and pestle, then sieved to retain 125 to 250 μm particles (W.S. TYLER No. 60 and No. 120 all-stainless-steel). Typically, 0.015-0.050 g of sieved Cu/SSZ-13 catalyst were mixed with enough inert silica gel (Fisher Chemical Silica Gel (Davisil) Sorbent, Grade 923) to obtain a bed height of ~ 0.5 cm. Aluminum foil was wrapped around the quartz reactor to an outer diameter of ~ 2.54 cm, in order to enhance heat conduction and minimize any radial temperature gradients that may be present within the bed. The reactor was then placed within a clamshell furnace (Applied Test Systems) and pressure-tested with helium (99.999%, Indiana Oxygen) at 5 psig for 20 minutes.

Steady state kinetic data were collected according to methods we have reported previously (17). Briefly, rate data were measured at differential NO conversion below 20% (total gas flow rate was varied between 0.8 to 1.5 L min^{-1}), to ensure the entire bed was exposed to approximately the same gas concentrations and temperatures using a gas mixture of 300 ppm NO (3.5% NO in Ar, Praxair), 300 ppm NH_3 (3.0% NH_3 in Ar, Praxair), 5% CO_2 (liquid, Indiana Oxygen), 10% O_2 (99.5%, Indiana Oxygen), 2.5% H_2O (deionized, introduced through 24" PermaPure MH Humidifier), and balance N_2 (boiloff liquid N_2 , Linde) at 473 K and 1 atm. The gas hourly space velocity (GHSV) was varied between 600,000 to 4,000,000 h^{-1} for all kinetic experiments. NO, NO_2 , NH_3 , CO_2 , N_2O , and H_2O concentration data were recorded every 0.95 seconds using a MKS MultiGas 2030 gas-phase Fourier transform infrared (FTIR) spectrometer with on-board calibrations. Reaction temperatures were collected using two Omega® K-type 1/16" OD thermocouples with one placed in contact with the top of the bed and the second placed in contact with the bottom of the bed. The temperature difference was always within 3 K during steady state SCR catalysis. Total gas flow rates were measured using a soap bubble flow meter.

In the limit of differential NO conversion, the gas concentrations and catalyst bed temperature can be assumed constant, allowing the NO consumption rate to be calculated using equation (S1):

$$-r_{NO}(\text{mol}_{NO} \text{ mol}_{Cu}^{-1} \text{ s}^{-1}) = \frac{(C_{NO,in} - C_{NO,out})}{1000000 \cdot \text{mol}_{Cu}} \dot{V}_{total} \left(\frac{P}{RT} \right) \quad (\text{S1})$$

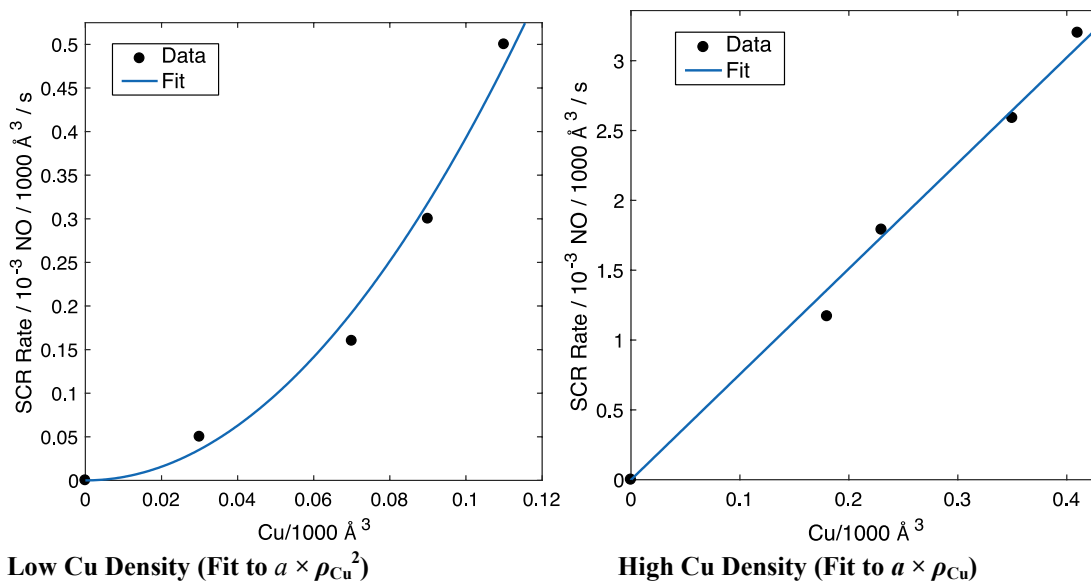
where C values are the concentrations of NO before and after the catalyst bed in ppm, \dot{V}_{total} is the total volumetric flow rate, P is 1 atm, T is ambient temperature, and R is the gas constant. The rate of NO consumption can further be converted from rate per Cu ($\text{mol NO mol Cu}^{-1} \text{ s}^{-1}$ or $\text{NO Cu}^{-1} \text{ s}^{-1}$) to rate per volume (molecules of NO consumed per 1000 $\text{\AA}^{-3} \text{ s}^{-1}$) using a multiplier for the number of Cu atoms per 1000 \AA^3 .

The experimental data are fitted to a power law rate expression where k_{app} is the apparent rate constant and α , β , and γ are the apparent reaction orders with respect to concentrations of NO, NH₃, and O₂, respectively.

$$-r_{NO} = k_{app} C_{NO}^{\alpha} C_{NH_3}^{\beta} C_{O_2}^{\gamma} \quad (S2)$$

$$k_{app} = A \exp\left(-\frac{E_{a,app}}{RT}\right) \quad (S3)$$

SCR rates measured as a function of Cu density (Cu-CHA catalysts depicted in figure 1 and table S3) were fit to two different models, as shown below. The four lowest Cu density samples were fit to rate = $a \times \rho_{Cu}^2$ (best fit $a = 39.3$, $R^2=0.99$) and the four highest Cu density samples to rate = $a \times \rho_{Cu}$ (best fit $a = 7.56$, $R^2=0.99$).



S3. X-ray Absorption Spectroscopy

X-ray absorption spectroscopy (XAS) experiments were performed at sector 10 MR-CAT (Materials Research Collaborative Access Team) of the Advanced Photon Source, Argonne National Laboratory. The insertion device beamline at sector 10 (10-ID) was used for the *operando* and *in situ* oxidation experiments due to the high photon flux available at that beamline. Incident and transmitted X-ray intensities were measured in ion chambers filled with 20% He in N₂ and 20% Ar in N₂, respectively, to obtain approximately 10% and 70% absorption of the beam before and after the sample, respectively. A Cu metal foil reference spectrum (edge energy of 8979 eV) was measured simultaneously with each sample spectrum to calibrate the X-ray beam for spectral measurements at the Cu-K edge. All sample spectra were normalized using 1st and 3rd order polynomials for background subtraction of the pre- and post-edges, respectively.

The Cu K-edge XANES spectra consists of several distinct features indicative of the various electronic transitions for the Cu^I and Cu^{II} oxidation states (43, 44). The peaks

at 8977 eV and 8987 eV are representative of Cu^{II}. The peak centered at 8977 eV is due to the symmetry forbidden 1s → 3d transition, which becomes allowed due to mixing of the 3d and 4p orbitals and has been reported in several studies as a low intensity, pre-edge feature (45-48). The shoulder at 8987 eV is due to the 1s → 4p electronic transition (49, 50). The presence of the sharp peak centered around 8983 eV is characteristic of the 1s → 4p transition for a two-coordinate Cu^I complex. This peak has previously been reported in the literature under a variety of environments including hydrocarbon SCR (51) and NO decomposition on Cu-ZSM-5 (52), thermal reduction of Cu-mordenite (53), Cu-Y (54), and two-coordinate Cu^I model compounds including copper(I) diamine complexes (37, 55, 56).

XAS is a bulk technique and each sample spectrum represents a mixture of oxidation states. Therefore, a linear combination XANES fitting of the Cu^I and Cu^{II} references was used to obtain the relative amounts of Cu in each oxidation state in a given spectrum. Information about how the Cu^I and Cu^{II} references were generated is provided in our previous publication (10). An absolute error of 5% was used as a conservative estimate for the uncertainty in the linear combination XANES fitting. The largest source of uncertainty is the Cu^I reference used in the fitting, as there is no specific Cu^I reference spectrum, and the choice of reference may not exactly reproduce the Cu^I amine structure present in the sample. If the Cu^I reference used in the fitting is assumed to be an accurate representation of the Cu^I structure present, the uncertainty in the linear combination XANES fitting would decrease to 2-3%.

The Debye-Waller factor (DWF) was determined to be 0.005 Å² for gas conditions that included NH₃, and was 0.003 Å² for all other gas conditions. All extended X-ray absorption fine structure (EXAFS) fitting was performed with the DWF fixed at the appropriate value, and EXAFS fitting was only performed on the first coordination shell of Cu-O. The k²-weighted data in R-space was fit by least-squares optimization to provide coordination numbers (CN) and interatomic bond distances. The EXAFS data was fit over k = 2.7 to ~8.5 Å⁻¹, incorporating as much data at high k values as possible.

Operando XAS

Operando experiments were performed in a special glassy carbon tube reactor, and the details of the custom *operando* XAS reactor setup were described by Kispersky et al. (39). During these experiments, XAS spectra were simultaneously collected while measuring the reaction rates for each sample to ensure that the standard SCR rate per mole Cu measured at APS were quantitatively the same, within error, to that measured in laboratory differential plug-flow reactors (PFR). Figure S20 shows standard SCR reaction rates measured on a representative sample (Cu-CHA-19) in the laboratory PFR and *operando* XAS reactor over a temperature range (450-480 K), indicating that rates are reproduced in the two reactor setups to within 10%. Table S5 shows that standard

SCR reaction rates for catalyst samples in the *operando* reactor described above are within 10% of those measured in a separate plug flow reactor, thus establishing kinetic equivalence of the two reactors.

In *operando* experiments, 7-13 mg of Cu-CHA-15, 30 mg of Cu-CHA-20, or 25 mg of Cu-CHA samples (sieved to 125-250 μm) were loaded in the *operando* reactor to maintain differential conditions ($< 20\%$ conversion). Gases were mixed and introduced into the reactor in a precise manner to avoid any side reactions. De-ionized H_2O was introduced into the feed stream by flowing He carrier gas through a heated shell type humidifier (Perma Pure MH-Series). All gas lines downstream of the humidifier were heated to above 373 K to prevent H_2O condensation. After introducing H_2O , NO (300 ppm in N_2 , Matheson Tri-Gas) was introduced into the gas stream, followed by the introduction of O_2 (20% in He, Airgas, Inc.). The reaction mixture was then preheated to 473 K. Ammonia (300 ppm in He, Airgas, Inc.) was introduced through a 1/16" stainless steel line that was located immediately upstream of the catalyst bed to minimize the possibility of gas-phase side reactions. Gas concentrations were measured using a MKS Multi-Gas 2030 gas analyzer FTIR with a cell temperature of 464 K and based on factory provided calibration files. Standard SCR conditions of 300 ppm NO, 300 ppm NH_3 , 10% O_2 , 2% H_2O , 5% CO_2 , a total flow rate of 1000-1200 mL min^{-1} and a temperature of 463-473 K was used for all steady state experiments. Steady state spectra were collected in the quick scan mode with an edge step of 0.5 eV, a dwell time of 0.05 s at each step and an energy range between 8700 and 9700 eV, with each spectrum taking 2-3 min to acquire. Steady state data were averaged over 3-5 scans depending on the data quality obtained under different experimental conditions. Linear combination XANES fits to determine the Cu^{I} and Cu^{II} fractions under *operando* conditions were carried out using the appropriate references, as explained in our previous publications (15, 17, 39).

Transient XAS

Transient O_2 and NO_2 oxidation experiments were carried out in the same flow reactor setup as used for *operando* experiments. Reduction with 300 ppm NO and 300 ppm NH_3 under a total flow of 1200 mL min^{-1} at approximately 447 K gave 90 ± 5 , 90 ± 5 and 98 ± 5 % Cu^{I} , for Cu-CHA-15, Cu-CHA-20, and Cu-CHA-29 samples, respectively. Following the reduction to Cu^{I} , samples were exposed to either 10% O_2 or 100 ppm NO_2 at the same temperature in separate experiments. The Cu^{I} and Cu^{II} fractions during these transient experiments were followed by collecting XANES spectra (Figures S6, S7, S8) in quick scan mode from 8800 to 9400 eV. Each spectrum took 21 s to acquire with a step size of 0.5 eV and a dwell time of 0.03 s. Higher quality spectra were collected at the end of these transients by increasing the dwell time from 0.03 s to 0.05 s. Linear combination XANES fits to determine the Cu^{I} and Cu^{II} fractions from spectra collected during transient experiments were performed using the same procedure to fit spectra collected during *operando* XAS experiments. The fitted Cu^{I} fraction before and at the end of O_2 and NO_2 oxidation transients are tabulated in Tables S6, S7, S8.

S4. Kinetic models for the transient oxidation experiments

O₂ oxidation of Cu^I(NH₃)₂

The transient O₂ data in Figure 3A were fit to a modified pseudo-second-order rate law described below. The approximate second-order behavior can be rationalized by postulating that the following termolecular reaction describes the oxidation of two Cu^I diamine complexes with O₂:



If this step were elementary and all sites behaved identically, the following rate law would describe the rate of consumption of Cu^I species:

$$\frac{d [\text{Cu}^{\text{I}}] (t)}{dt} = -2k_a ([\text{Cu}^{\text{I}}] (t))^2 [\text{O}_2] \quad (\text{S5})$$

Because O₂ is in stoichiometric excess during these transient experiments, its concentration can be subsumed into k_a and the above expression can be rewritten as:

$$\frac{d [\text{Cu}^{\text{I}}] (t)}{dt} = -2k ([\text{Cu}^{\text{I}}] (t))^2 \quad (\text{S6})$$

where k is a pseudo-second-order rate constant. To correct for the unoxidizable, recalcitrant fraction of Cu^I (defined as [Cu^I]_∞) in the transient O₂ experiments (Figure 3A), we introduce the transformation:

$$\begin{aligned} [\text{Cu}^{\text{I}}]_{\text{corr}} (t) &= [\text{Cu}^{\text{I}}] (t) - [\text{Cu}^{\text{I}}]_{\infty} \\ \frac{d [\text{Cu}^{\text{I}}]_{\text{corr}} (t)}{dt} &= -2k ([\text{Cu}^{\text{I}}]_{\text{corr}} (t))^2 \end{aligned} \quad (\text{S7})$$

[Cu^I]_{corr}(t) is defined as the concentration of oxidizable Cu^I (by O₂) as a function of time during the transient O₂ experiment. Integrating from 0 to t and rearranging:

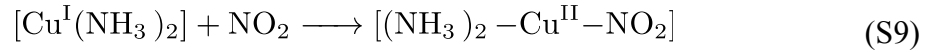
$$\text{Cu}^{\text{I}} \text{ Fraction} = \frac{[\text{Cu}^{\text{I}}] (t)}{[\text{Cu}^{\text{I}}]_0} = \frac{1 - [\text{Cu}^{\text{I}}]_{\infty}/[\text{Cu}^{\text{I}}]_0}{1 + 2k ([\text{Cu}^{\text{I}}]_0 - [\text{Cu}^{\text{I}}]_{\infty}) t} + \frac{[\text{Cu}^{\text{I}}]_{\infty}}{[\text{Cu}^{\text{I}}]_0} \quad (\text{S8})$$

where Cu^I Fraction is the time-dependent Cu^I concentration divided by the initial Cu^I concentration ([Cu^I]₀). The parameters in Eqn. S8 are k and [Cu^I]_∞. For each data series, we set [Cu^I]_∞ to the last (longest time) Cu^I Fraction data point, and used nonlinear least-squares regression to obtain the best-fit parameter of k . Results are summarized below:

	Cu-CHA-29	Cu-CHA-20	Cu-CHA-15
$k(\text{m}^3 \text{ mol Cu}^{-1} \text{ s}^{-1})$	0.00011	0.00017	0.00082
$[\text{Cu}^{\text{I}}]_{\infty} / [\text{Cu}^{\text{I}}]_0$	0.26	0.10	0.05
R^2	0.99	0.98	0.99

NO₂ oxidation of Cu^I(NH₃)₂

The transient NO₂ data in Figure S13 were fit to a pseudo-first-order rate law described below. The first-order behavior can be rationalized if we postulate that the observed oxidation kinetics are governed by the bimolecular reaction of a single Cu^I diamine with NO₂:



If this reaction is elementary, then the rate law that describes the rate of consumption of Cu^I species is:

$$\frac{d[\text{Cu}^{\text{I}}](t)}{dt} = -k_a [\text{Cu}^{\text{I}}](t) [\text{NO}_2] \quad (\text{S10})$$

Because NO₂ is in stoichiometric excess during these transient experiments, its concentration can be subsumed into k_a and the above expression rewritten as:

$$\frac{d[\text{Cu}^{\text{I}}](t)}{dt} = -k [\text{Cu}^{\text{I}}](t) \quad (\text{S11})$$

Upon integration and rearranging, the above expression becomes:

$$\text{Cu}^{\text{I}} \text{ Fraction} = \frac{[\text{Cu}^{\text{I}}](t)}{[\text{Cu}^{\text{I}}]_0} = e^{-kt} \quad (\text{S12})$$

where Cu^I Fraction and $[\text{Cu}^{\text{I}}](t)$ and $[\text{Cu}^{\text{I}}]_0$ are defined in the same way as reported in the previous subsection. The only unknown parameter in Eqn. S11 is k . Nonlinear least-squares regression was used to obtain the best-fit k value from the data in Figure S13. The results are summarized below:

	Cu-CHA-29	Cu-CHA-20	Cu-CHA-15
$k(\text{s}^{-1})$	0.026	0.028	0.030
R^2	0.98	0.98	0.89

S5. DFT Methods

To construct the energy landscape for Cu diffusion through an 8-MR and reaction with O₂ we calculated the energies of structures for A through E in Figure 4 using the

following protocol. All structures are attached to the supplementary information in CONTCAR format in the file CONTCARs.zip.

Due to the dynamic and mobile nature of solvated Cu species in the zeolite cage, we used AIMD on all structures to seek low energy configurations. A 12 T-site supercell containing two Al atoms was used for Fig. 4 structures C and D, such that each Cu charge compensates 1Al. For Fig. 4 structure A, the 12 T-site supercell was doubled to create a 24 T-site supercell, so that each $\text{Cu}^{\text{I}}(\text{NH}_3)_2$ can occupy one CHA cage. Multiple initial structures were guessed, and each geometry was sampled by Born-Oppenheimer molecular dynamics in the canonical ensemble (NVT) using the Car-Parrinello Molecular Dynamics (CPMD) software version 3.17.1 (57). We used the Perdew-Becke-Erzenhof (PBE) (58) flavor of the generalized gradient approximation (GGA) exchange-correlation functionals and Vanderbilt ultrasoft pseudopotentials (59), and a plane wave cutoff of 30 Ry. The first Brillouin zone was sampled at the Γ point only for this insulator, and a Nose-Hoover thermostat was used to achieve the target temperature of 473 K. A 0.6 fs time step was used for a total sampling time of 150 ps, for each of structures A, C and D in Figure 4. Structures B and E came from guessing product structures for the Climbing Image Nudged Elastic Band (CI-NEB) calculations described below and were not sampled by AIMD.

Next, for structures A, C, and D, we selected several (3 to 4) low energy structures from the 150 ps of AIMD trajectories and performed electronic energy optimizations using the Vienna Ab initio Simulation Package (VASP) version 5.4.1 (60) and the same supercell. Periodic DFT calculations were performed using the projector augmented wave (PAW) method with the PBE functional (58) and a 400 eV plane wave cutoff, and DFT-D2 (61) to calculate van der Waals dispersion energies. Electronic energies were converged self-consistently to less than 10^{-8} eV, and forces to less than $0.01 \text{ eV}/\text{\AA}$, on each atom. For the above calculations, PBE POTCARs for each atom were used. We performed spin-polarized calculations for Cu dimers to sample both the singlet and triplet state of the dimers. The lower energy structure was chosen and plotted on Figure 4 and reported in Table S10. Structures A, B, D and E are in singlet states and structure C is in triplet state. All structures in Figure 4 are attached to the SI in CONTCAR format.

Transition states (A to B, and D to E) were computed using the Climbing Image Nudged Elastic Band (CI-NEB) method (62) and the same functional and plane wave cutoff described above. Convergence criteria were tightened to less than 10^{-8} eV for electronic energy and less than $0.01 \text{ eV}/\text{\AA}$ for force on each atom. The transition state from C to D is spin forbidden and was not computed here; we estimated the effective barrier from the literature as reported in Figure 4.

We followed a similar protocol for reactions of one $\text{Cu}^{\text{I}}(\text{NH}_3)_2$ with O_2 and NO_2 . We first performed 150 ps of AIMD for O_2 and NO_2 adsorption on $\text{Cu}^{\text{I}}(\text{NH}_3)_2$, using a 12 T-site supercell with 1 Al, and with the CPMD software. Low energy structures were then selected and optimized (spin polarized) with both PBE/DFT-D2 and the hybrid screened-exchange Heyd-Scuseria-Ernzerhof (HSE06) functionals (63) with the

Tkatchenko Scheffier method (TSvdW) (64) to correct for dispersion interactions. We performed these additional HSE06-TSvdw calculations because hybrid functionals have been shown to predict NO_x adsorption energies more accurately than GGA functionals (12). Figure S14 and Table S10 reports the structures and adsorption energies.

S6. NO titrations to probe reaction stoichiometry

The consumption of NO (per Cu) in sequential SCR reaction steps on Cu-CHA zeolites was measured and used to corroborate the reaction stoichiometry depicted in Figure 6. Typically, 10 to 20 mg of sample was loaded into the reactor system used to measure steady-state SCR kinetics. The total gas flow rate used in the following procedure was 600 mL min⁻¹. The samples in Figure 3A were first oxidized and dehydrated to their Cu^{II} form (10) by treatment to 823 K (0.167 K s⁻¹) in flowing 20% O₂ (99.5%, Indiana Oxygen) in balance He (99.999%, Indiana Oxygen), and then cooling to 473 K. The sample was then held flowing He for 30 minutes, and then fully reduced in a mixture of 300 ppm NO (3.5% NO in Ar, Praxair) and 300 ppm NH₃ (3.0% NH₃ in Ar, Praxair) in balance He. Following reduction of Cu sites to their Cu^I(NH₃)₂ states (corresponding to 6 o'clock positions in Figure 6), the samples were exposed to flowing 10% O₂ in balance He until steady-state was achieved (corresponding to the central position in Figure 6). The O₂ oxidized sample was then held in a flowing stream of 300 ppm of NO in balance He, until steady-state was achieved. Finally, 300 ppm NH₃ was introduced to the flow of NO in balance He, to reduce the sample back to Cu^I(NH₃)₂ (corresponding to 6 o'clock positions in Figure 6). Each of these sequential treatments was also performed in a blank reactor to measure a baseline signal in the FTIR spectrometer (MKS Multigas TM 2030) used to account for gas holdup and residence time in the reactor setup (NO conversion was not detected in the blank reactor), in order to calculate the NO consumption from the Cu-CHA catalyst during each treatment step (Figure S12).

Summarizing, after O₂ oxidation of Cu^I(NH₃)₂ to form a NH₃-solvated Cu^{II} dimer (central position in Figure 6), the two-step procedure described above exposes the catalyst to NO alone, and then to NO and NH₃ together. Exposure of NO in the step immediately following O₂-assisted oxidation results in the consumption of one NO equivalent (NO:Cu = 0.98 ± 0.10) per Cu site. Once steady-state is achieved, the sequential addition of NH₃ to the flowing stream (already containing NO) consumes another equivalent of NO per Cu site (NO:Cu = 1.07 ± 0.11) and fully reduces the sample to Cu^I(NH₃)₂ (6 o'clock positions in Figure 6), which closes the catalytic cycle. The 2:1 NO:Cu consumption ratio is consistent with Figure 6. Starting from the Cu-oxo dimer in the center of the Figure 6, two NO molecules per Cu are required to return to the 6 o'clock position in each cycle corresponding to the formation of Cu^I(NH₃)₂ species.

S7. Random Distribution of Cu per Cage

To eliminate the possibility that the oxidizable fraction of Cu^I corresponds to Cu pairs or larger aggregates that, by random chance, are present in the same cage and not from pairs formed from mobile Cu^I ions, we estimated the fraction of persistent pairs that

would be present assuming that Cu are randomly distributed among cages. Results are compared with the observed fraction of oxidizable Cu^{I} in Figure S15. For Cu densities corresponding to the zeolites studied in Figure 3, this “immobile Cu dimer” model predicts values that are much smaller than the $[\text{Cu}^{\text{I}}]_{\infty}$ values observed experimentally and predicted from the non-mean-field model described in S10:

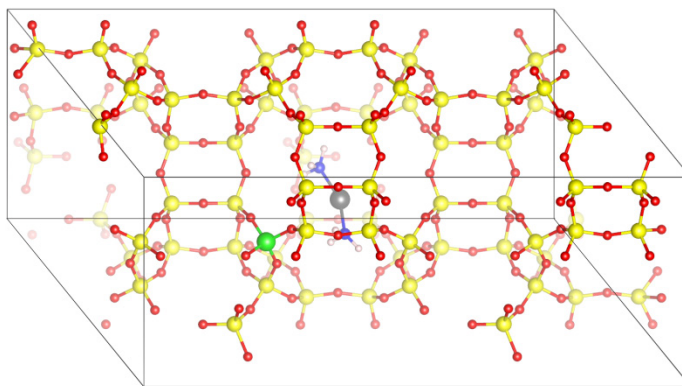
Cu-CHA-15: Oxidizable Cu Fraction = 0.072, $[\text{Cu}^{\text{I}}]_{\infty}/[\text{Cu}^{\text{I}}]_0 = 0.928$

Cu-CHA-20: Oxidizable Cu Fraction = 0.012, $[\text{Cu}^{\text{I}}]_{\infty}/[\text{Cu}^{\text{I}}]_0 = 0.988$

Cu-CHA-29: Oxidizable Cu Fraction = 0.002, $[\text{Cu}^{\text{I}}]_{\infty}/[\text{Cu}^{\text{I}}]_0 = 0.998$

S8. Metadynamics

We used metadynamics to compute the free energy landscape for a $\text{Cu}^{\text{I}}(\text{NH}_3)_2$ to diffuse away from a charge-compensating Al center into an adjacent cage. To avoid interaction between periodic cells, a CHA supercell with 72 T-sites was adopted. The 72-T-site supercell (pictured below) was generated by propagating the 36 T-site CHA-silica supercell obtained from the database of zeolite structures (36) along one direction. A T-site silicon is replaced by aluminum and a $\text{Cu}^{\text{I}}(\text{NH}_3)_2$ complex was inserted into a cage near the Al to create the initial $\text{Cu}^{\text{I}}(\text{NH}_3)_2$ structure.



72-T site supercell for metadynamics simulation. Color code for different elements in superimposed figure: gray=Cu, green=Al, yellow=Si, red=O, blue=N and white=H.

All calculations were performed in the CPMD program (57). 6 ps of *NVT* molecular dynamics were run to pre-equilibrate the system. The *NVT* MD simulation was initiated by quenching the system to the non-spin-polarized Born–Oppenheimer potential surface with the Perdew–Becke–Erzenhof generalized gradient approximation (GGA) exchange–correlation functional (58) and ultrasoft pseudopotentials (59). Plane waves were included up to 30 Rydberg and the Brillouin zone sampled at the Γ point. Self-consistent-field (SCF) electronic energies were converged to 1×10^{-7} Ha. The converged wavefunction was subsequently used to perform Car–Parrinello molecular dynamics (57) (CPMD) at 473 K with a time step of 0.12 fs. A Nose–Hoover thermostat

was used for both ions and electrons. The electronic temperature was set to 0.02 K with frequency 10000 cm^{-1} . The fictitious electron mass was set to 400 atomic unit.

The pre-equilibrated structure, wavefunction, atomic velocities and thermostat were used for the subsequent metadynamics (65, 66) simulation with a total simulation time of 12.5 ps. The time step and thermostat setting were the same as those in the MD simulation. The collective variable was chosen to be the Cu-Al coordination number (CN), defined as

$$CN = \frac{1 - \left(\frac{d_{ij}}{d_0}\right)^p}{1 - \left(\frac{d_{ij}}{d_0}\right)^{p+q}} \quad (\text{S13})$$

where d_{ij} is defined as distance between Al and Cu and p and q are arbitrary scaling constants. Values of other parameters are summarized in Table S11. d_0 was chosen as largest Cu-Al separation distance observed in the regular NVT MD simulation at 473 K. The k and μ were chosen such that the Lagrangian collective variable s and the physical collective variable S stay close, and that S fluctuates frequently at each position in the configuration space.

S9. Electrostatics

We estimated the electrostatic interaction between a Cu^{I} ion and its charge-compensating Al center using Coulomb's Law. We assumed Cu and Al to be elementary positive and negative point charges, respectively, carrying the same electric charge as a proton, $1.6 \times 10^{-19} \text{ C}$, and we used the computed dielectric constant of CHA-zeolite (ϵ_r), 2.7, reported by Rybicki and Sauer (67). The equilibrium Cu-Al distance of 4.6 Å taken from the DFT-optimized $\text{Cu}^{\text{I}}(\text{NH}_3)_2$ structure was used as the initial Cu-Al distance in the calculation. The energy of ionic separation of Cu^{I} and framework Al from 4.6 Å to r was calculated following Coulomb's law:

$$F = \frac{k_e q_{\text{Cu}} q_{\text{Al}}}{\epsilon_r r^2} \quad (\text{S14})$$

$$\Delta E = N_a \int_{4.6\text{\AA}}^r F dr^* \quad (\text{S15})$$

where k_e is the electric force constant in vacuum, N_a is the Avogadro constant, ϵ_r is dielectric constant of CHA-zeolite, q_{Cu} and q_{Al} are Cu and Al charges, and r is the Cu-Al distance.

The computed Coulombic potential as a function of Cu-Al distance was plotted and compared with the metadynamics-computed free energy profile in Figure 5. The Coulombic potential and the computed free energy are similar up to 7 Å, consistent with electrostatics dominating the interaction. The computed free energy is slightly more positive than the Coulombic potential for Cu-Al distance between 7 Å and 8 Å, highlighting the activation barrier for $\text{Cu}^{\text{I}}(\text{NH}_3)_2$ to travel through an 8-member-ring

window to a neighboring CHA cage, which is not captured by the Coulombic model. The computed free energy falls after $\text{Cu}^{\text{I}}(\text{NH}_3)_2$ reaches the new cage and stays relatively invariant thereafter. The Coulombic potential continues to increase rapidly and surpasses the computed free energy above 8 Å. Such difference can be rationalized by many-body long range Coulombic interaction between $\text{Cu}^{\text{I}}(\text{NH}_3)_2$ and framework Al in periodic images in the metadynamics simulation, which intrinsically lower the computed free energy compared to a two-point-charge Coulombic model.

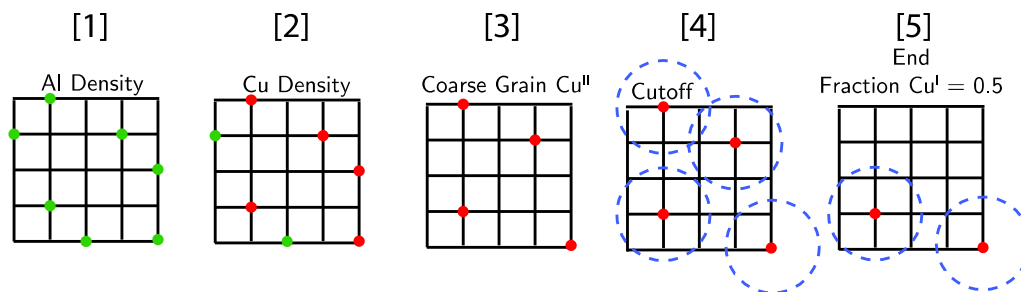
S10. Stochastic Simulation

Here, we estimate the fraction of Cu^{I} able to form an oxo-bridged dimer (Figure 4), given a density of Cu and Al atoms in a CHA zeolite and a maximum distance that each Cu can diffuse from its charge compensating Al. Cu number densities between 7×10^{-4} and 0.99 Cu/1000 Å³ and Cu-Al diffusion distances (represented by the green spheres in Figure 3B) from 5-12.5 Å were modeled (Figure S16); procedural details are described below.

We use a 1536 T-site CHA periodic supercell (36) with a total volume of 1.0172×10^5 Å³. The large cell size was used to avoid bias due to an even or odd number of exchanged Cu present at smaller cell sizes and long Cu diffusion distances. We performed stochastic simulations as a function of Si/Al (spanning 2 to 511), Cu/Al (0.0059 to 1), and a maximum Cu diffusion distance of 12.5 Å from the compensating framework Al atom.

A 2D schematic representation of the simulation scheme is shown below; the actual simulation was carried out on the 3D CHA lattice described above. In step [1], CHA T-sites were randomly populated with Al avoiding any Al-Al first-nearest-neighbors (Loewenstein's rule) (33). In step [2], we associated Cu ions with these Al, obeying the previously validated rule (10) that 2Al 6MR sites first exchange Cu^{II} before remaining 1Al sites exchange $\text{Cu}^{\text{II}}\text{OH}$. Three types of Al exist at this point: those that are not associated with a Cu ion, those that compensate a $\text{Cu}^{\text{II}}\text{OH}$, and 2Al 6MR sites that share a Cu^{II} . In step [3], we delete from the lattice the Cu-free Al sites and one member of every Al pair that compensate a Cu^{II} ion. In step [4], we created an Al-Al neighbor list, including only neighbors that are within twice the prescribed Cu diffusion radius. In step [5], we then deleted overlapping pairs at random from the neighbor list, stopping when the number of available pairs vanishes. We recorded the number of remaining entries divided by the initial number of Cu as the Cu^{I} fraction. The simulation was then repeated until the average Cu^{I} fraction converged.

As we explored different Si/Al and Cu/Al ratios, we discovered that results were sensitive to total initial Cu^{I} density and insensitive to the underlying Si/Al and Cu/Al ratios. Results are shown in Figure S16, plotted as final Cu^{I} fraction vs initial Cu^{I} density, for a range of diffusion distances. Simulation results are of course discrete; for visual convenience we present the data using cubic spline interpolation. A diffusion distance of 9 Å, consistent with predictions from the metadynamics simulation (Figure 5), predicts final Cu^{I} fractions in close agreement with experimental observation (Figure 3A).



To provide a visual representation of the simulation results, we took a snapshot of steps [3] and [5] for one simulation iteration at the initial Cu densities for the Cu-CHA zeolites represented in Figure 3A. Cartesian coordinates of Al charge compensated by Cu were extracted from the stochastic simulations and green spheres 9 Å in radius were plotted, representing the maximum diffusion length of each $\text{Cu}^{\text{I}}(\text{NH}_3)_2$ (Figure 3B, $t=0$). Spheres are translucent so that overlapping spheres are easily visualized and periodic boundary conditions used to show the diffusion range of Cu across the supercell boundaries. Intersecting spheres around Cu coordinates were plotted both before step [3] and after step [5] pairing to show the geometrically isolated Cu (Iso) and statistically isolated “musical chairs” Cu (MC).

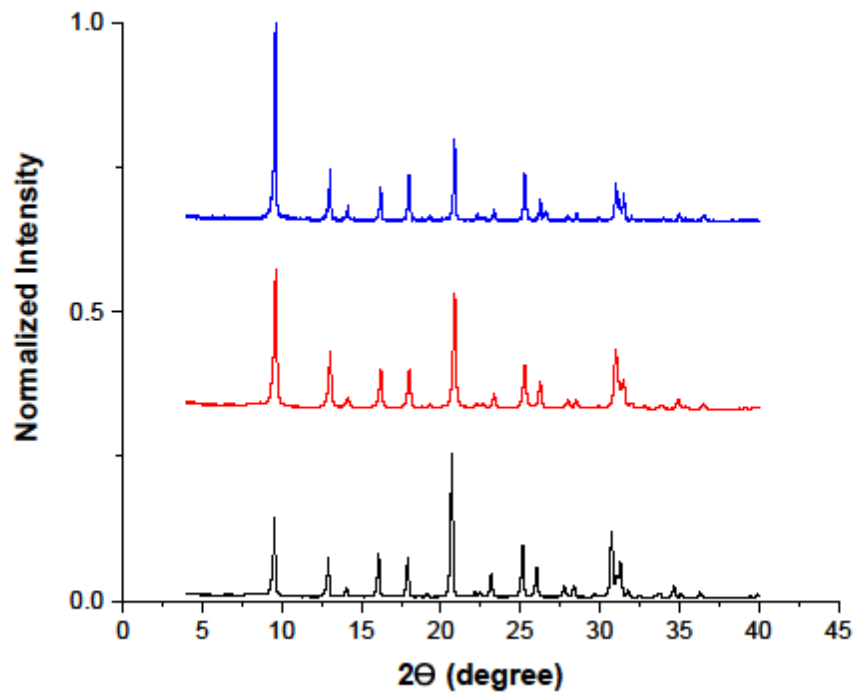


Fig. S1. X-Ray diffraction patterns of H-SSZ-13 zeolites with Si/Al = 4.5 (blue), Si/Al = 15 (red), and Si/Al = 25 (black), measured using a Cu K-alpha source ($\lambda = 0.154$ nm). Diffraction patterns are vertically offset for clarity. Cu-exchanged forms of these materials show equivalent XRD patterns (68).

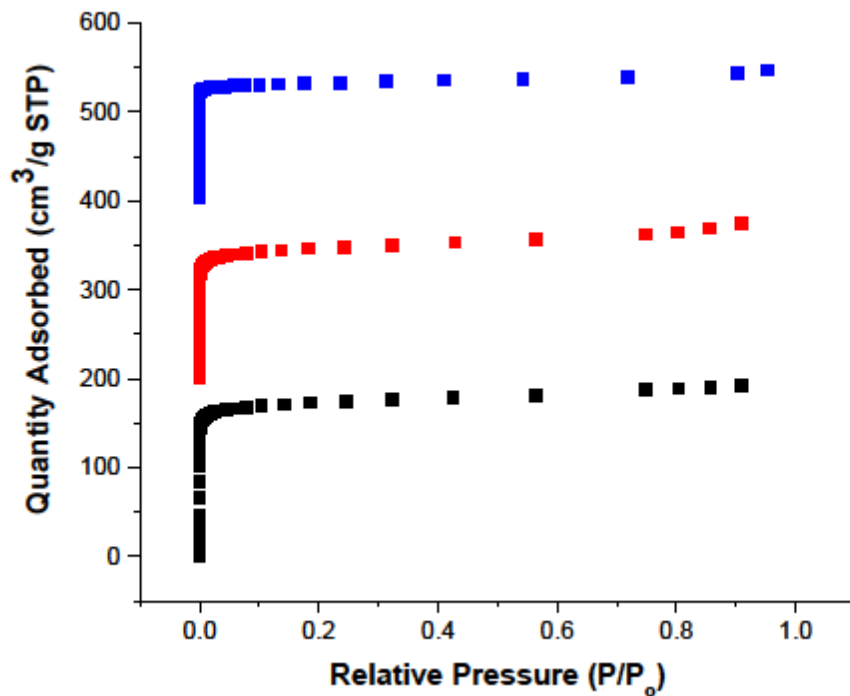


Fig. S2. Ar adsorption isotherms on H-SSZ-13 with Si/Al = 4.5 (blue), Si/Al = 15 (red), and Si/Al = 25 (black). Isotherms are vertically offset for clarity (Si/Al=15: by 200 cm³ g⁻¹, Si/Al=25: by 400 cm³ g⁻¹). Cu-exchanged forms of these materials show similar adsorption isotherms, with slight decreases in micropore volumes caused by the presence of Cu (68).

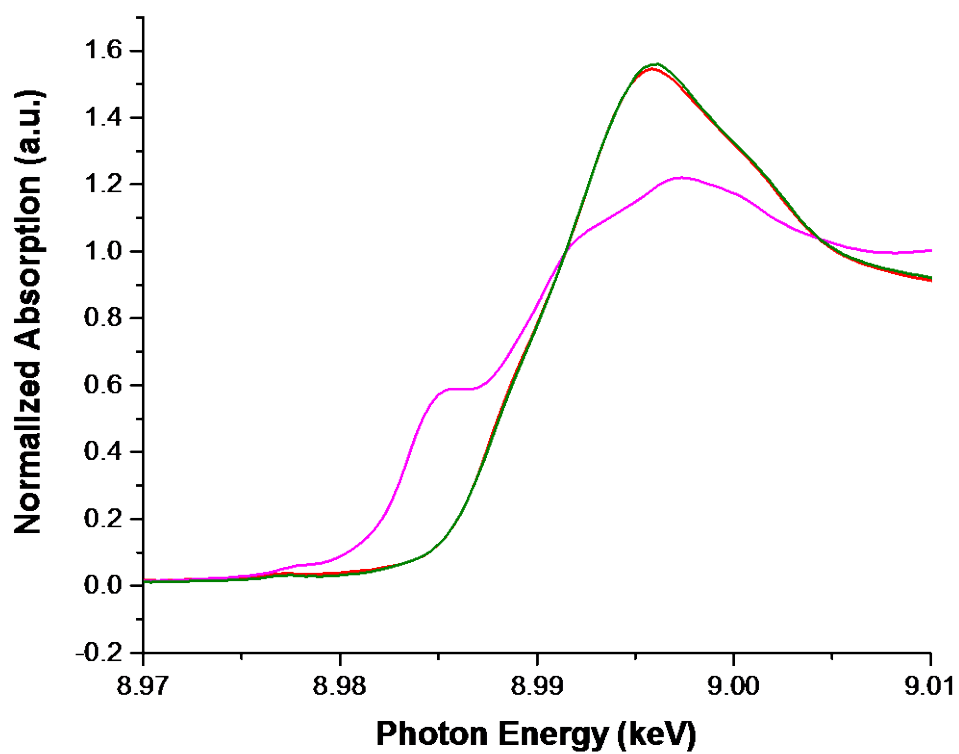


Fig. S3. XANES spectra for Cu-CHA-20 (red) and Cu-CHA-29 (green) at ambient conditions, and for bulk Cu^{II}O (pink).

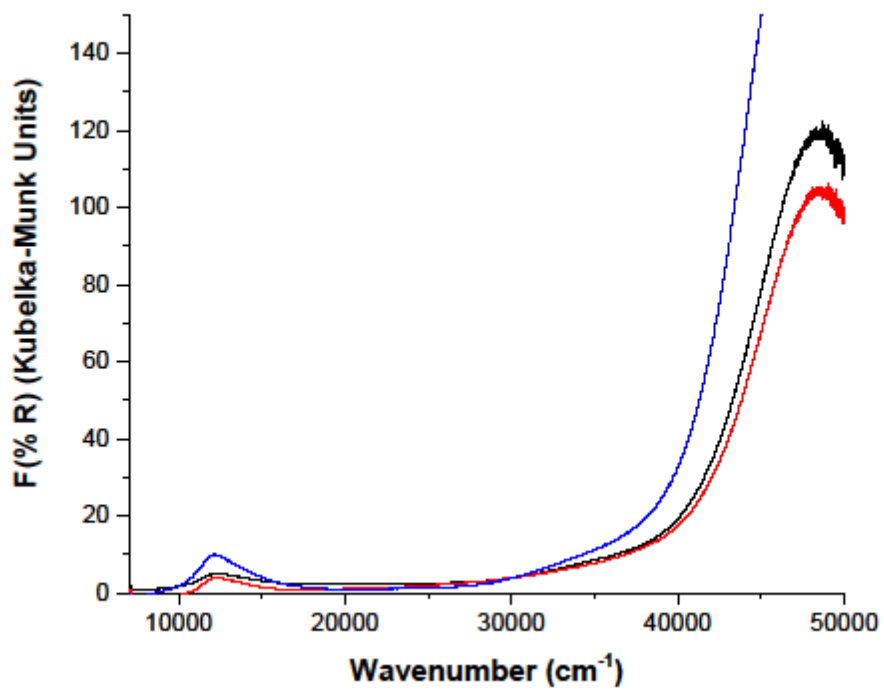


Fig. S4. UV-Vis spectra for Cu-CHA-15 (blue), Cu-CHA-20 (black), and Cu-CHA-29 samples (red) recorded at ambient conditions.

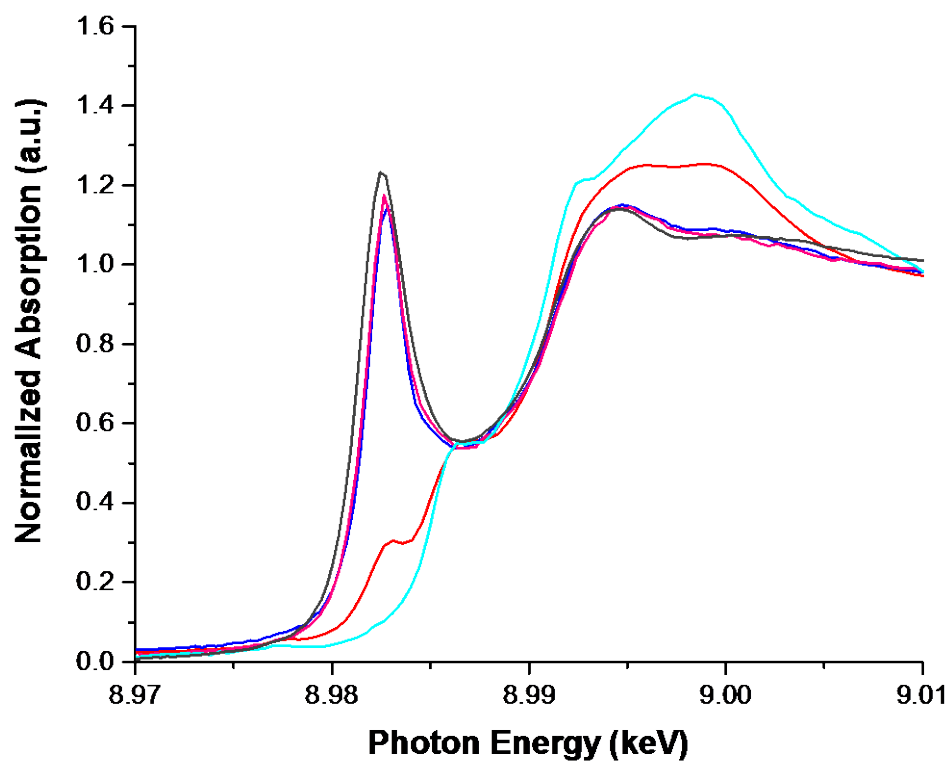


Fig. S5. *Operando* XANES spectra of Cu-CHA-15 (red) and Cu-CHA-29 (dark blue) during steady-state standard SCR (300 ppm NO, 300 ppm NH₃, 10% O₂, 2% H₂O, 5% CO₂, 463-473 K). Reference spectra for aqueous Cu^I(NH₃)₂ (grey), isolated Cu^I (10) (pink) and isolated Cu^{II} (light blue) sites (10).

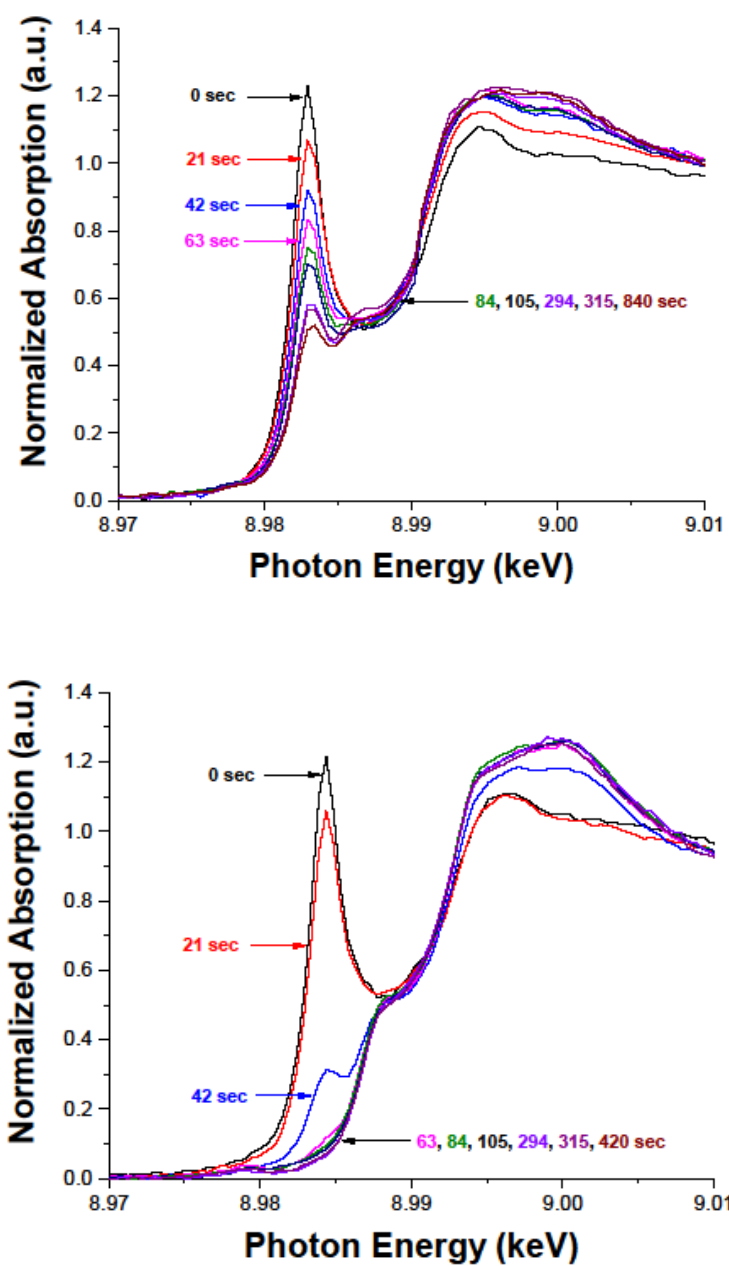


Fig. S6. XANES spectra collected during transient oxidation of the reduced forms of Cu-CHA-29 sample with 10% O₂ (top) and 100 ppm NO₂ (bottom), as a function of time (labeled in figure).

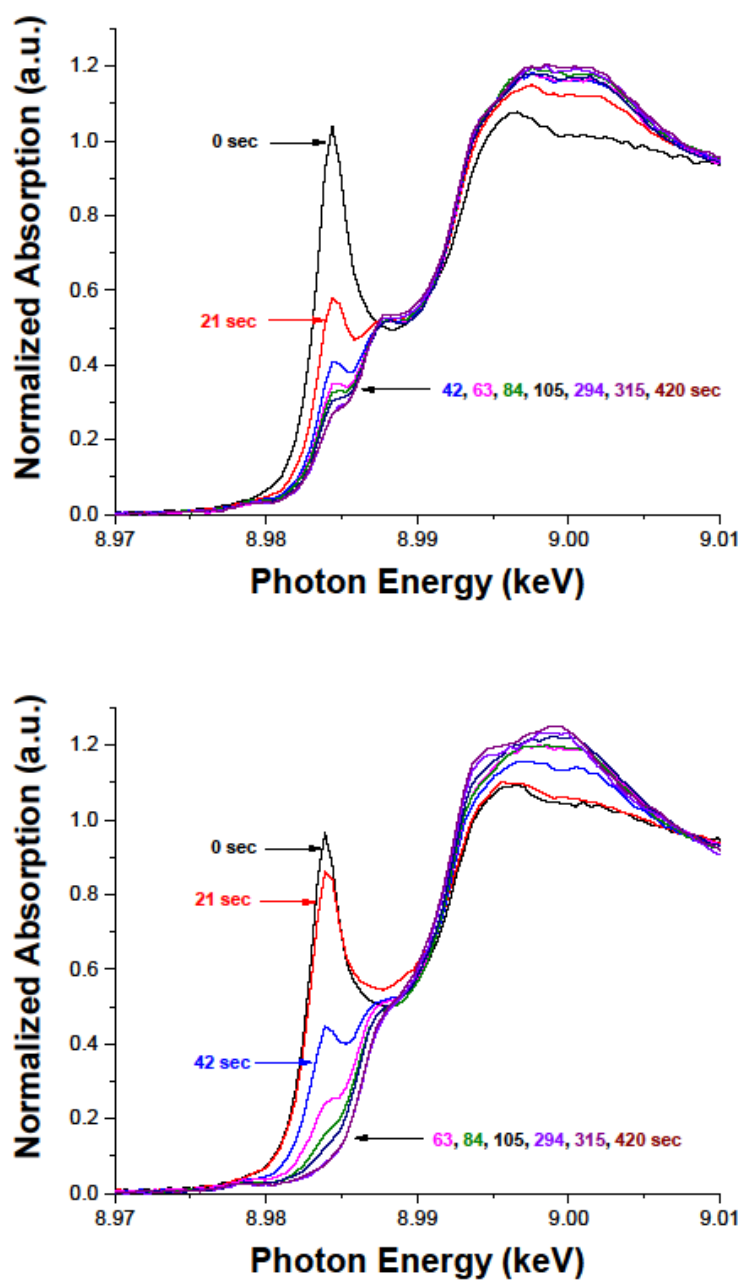


Fig. S7. XANES spectra during transient oxidation of the reduced forms of Cu-CHA-20 sample with 10% O₂ (top) and 100 ppm NO₂ (bottom), as a function of time (labeled in figure).

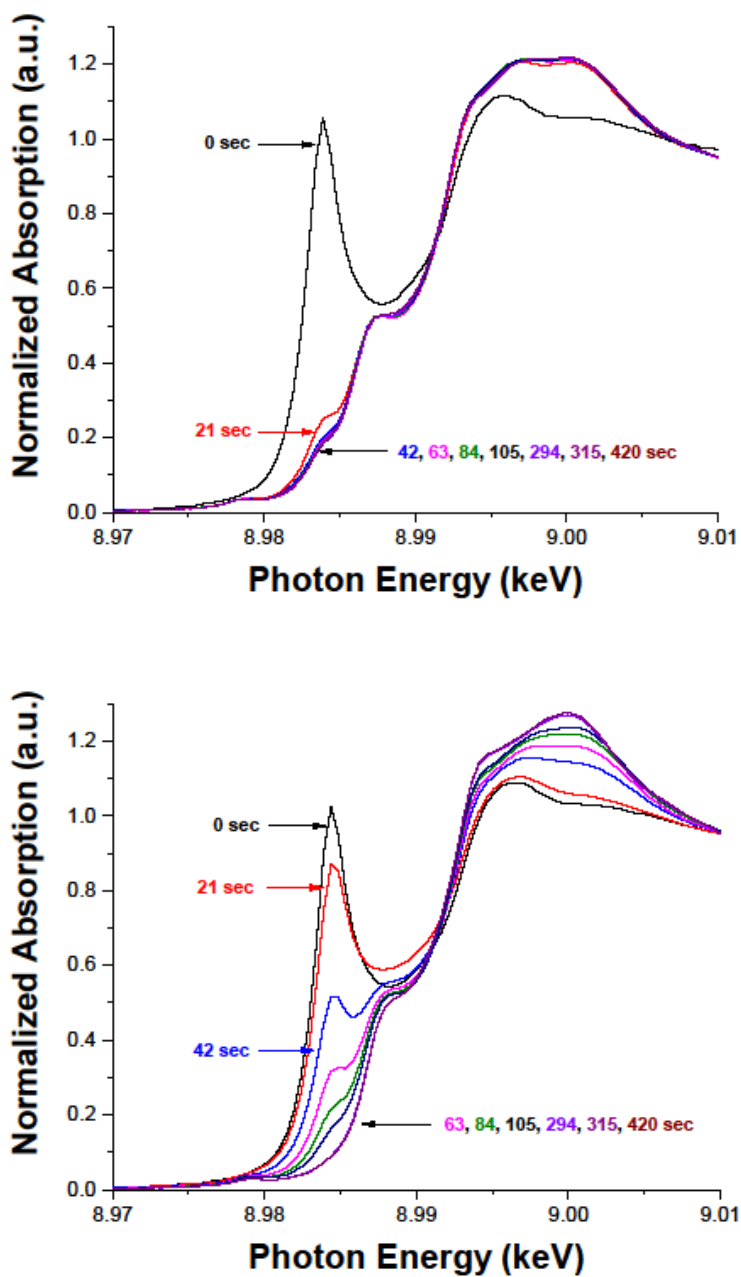


Fig. S8. XANES spectra during transient oxidation of the reduced forms of Cu-CHA-15 sample with 10% O₂ (top) and 100 ppm NO₂ (bottom), as a function of time (labeled in figure).

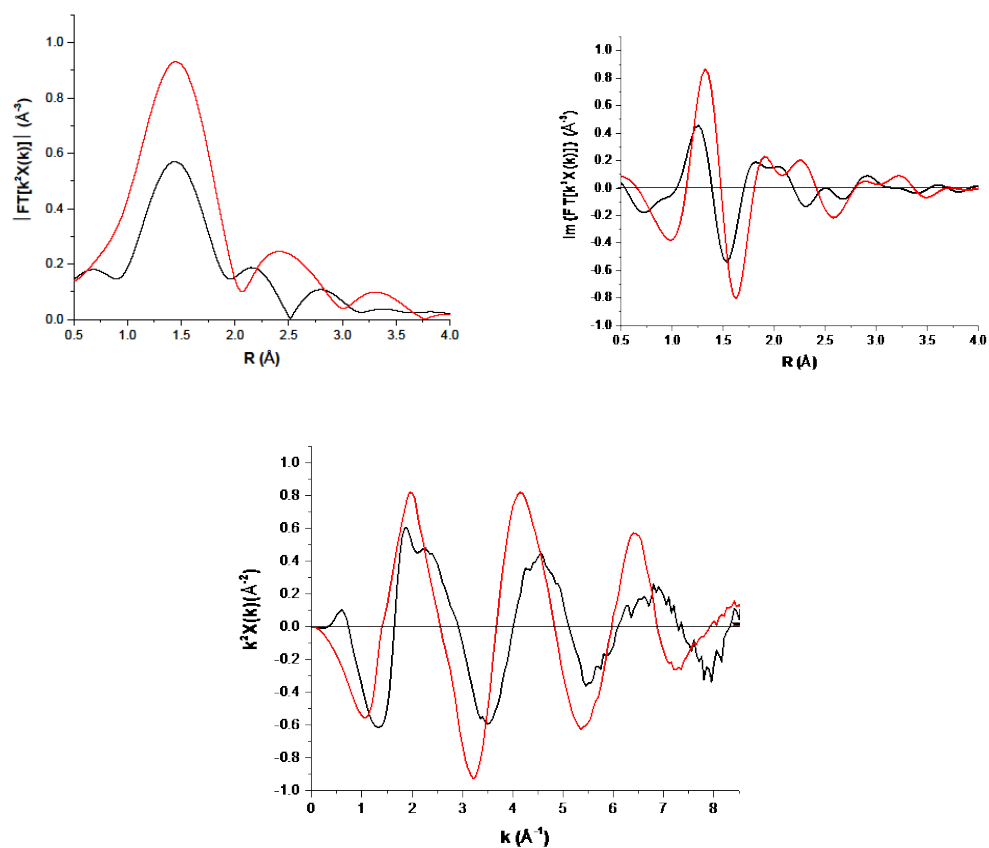


Fig. S9. The k^2 weighted Fourier transform (moduli and imaginary parts of FT on top left and top right, respectively) and raw EXAFS spectra (bottom) collected before (black) and after (red) oxidation with 10% O_2 at 473 K, starting from the reduced $Cu(I)(NH_3)_2$ state of Cu-CHA-29.

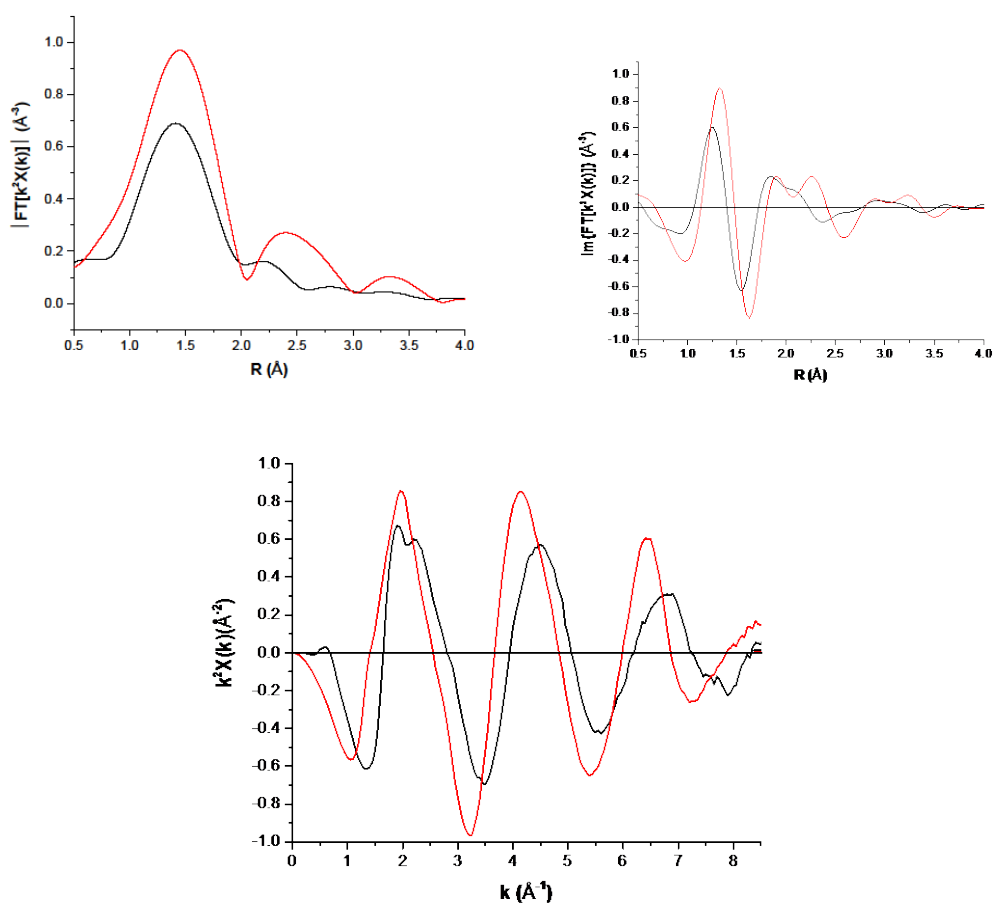


Fig. S10. The k^2 weighted Fourier transform (moduli and imaginary parts of FT on top left and top right, respectively) and raw EXAFS spectra (bottom) collected before (black) and after (red) oxidation with 10% O_2 at 473 K, starting from the reduced $Cu(I)(NH_3)_2$ state of Cu-CHA-20.

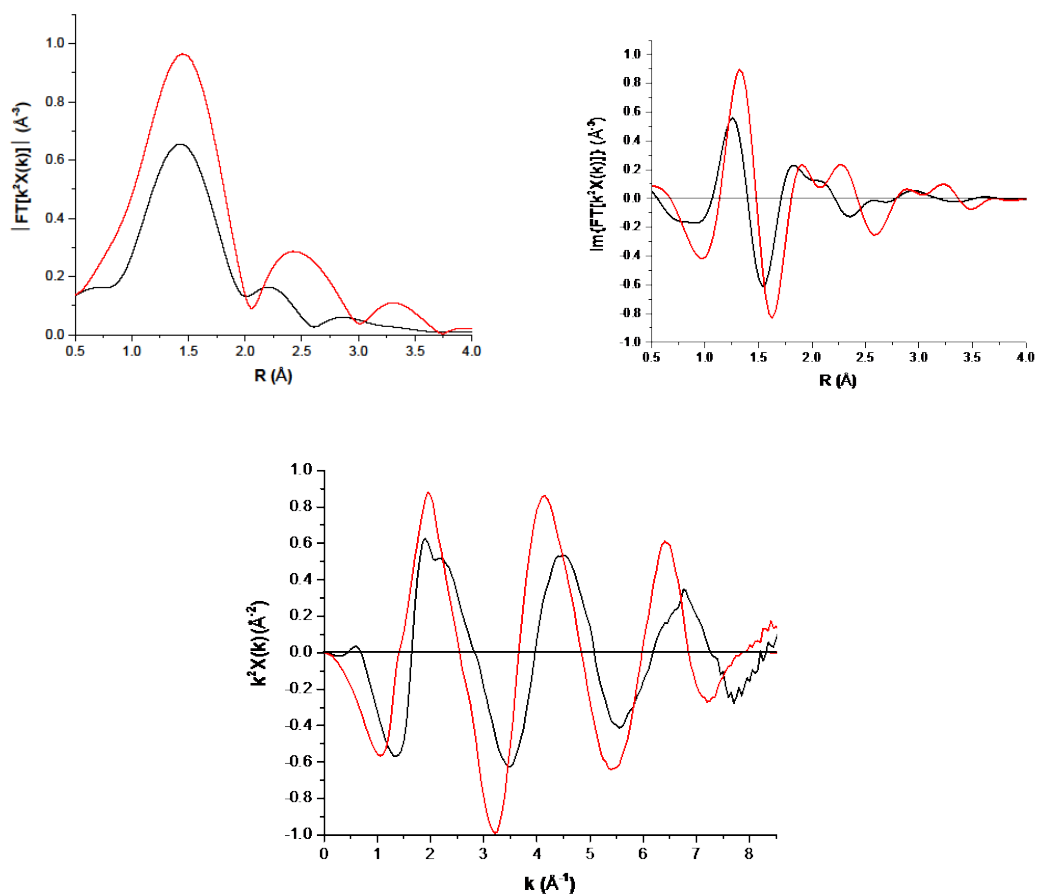


Fig. S11. The k^2 weighted Fourier transform (moduli and imaginary parts of FT on top left and top right, respectively) and raw EXAFS spectra (bottom) collected before (black) and after (red) oxidation with 10% O_2 at 473 K, starting from the reduced $Cu(I)(NH_3)_2$ state of Cu-CHA-15.

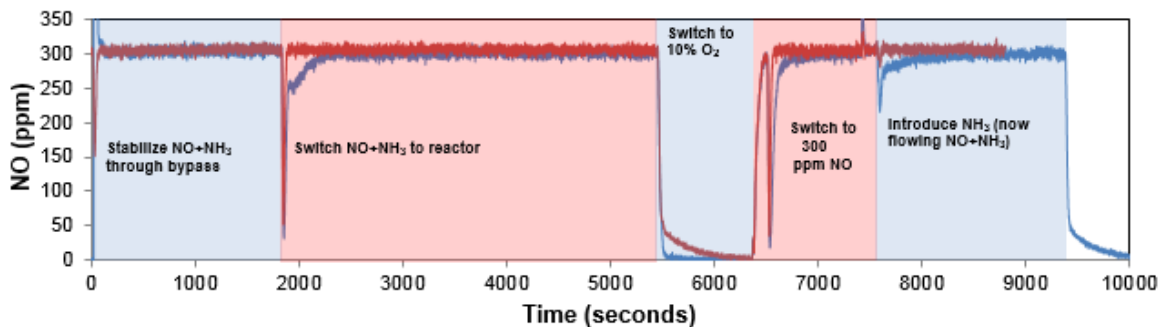


Fig. S12. NO concentrations measured in the reactor effluent during five step-wise treatments of Cu-CHA-15, in order to quantify NO consumption (per Cu) in treatment steps 2, 4, and 5 above, which correspond to different steps in the proposed standard SCR cycle (Figure 6). Red and blue traces indicate experiments with the blank reactor and catalyst-loaded reactor, respectively.

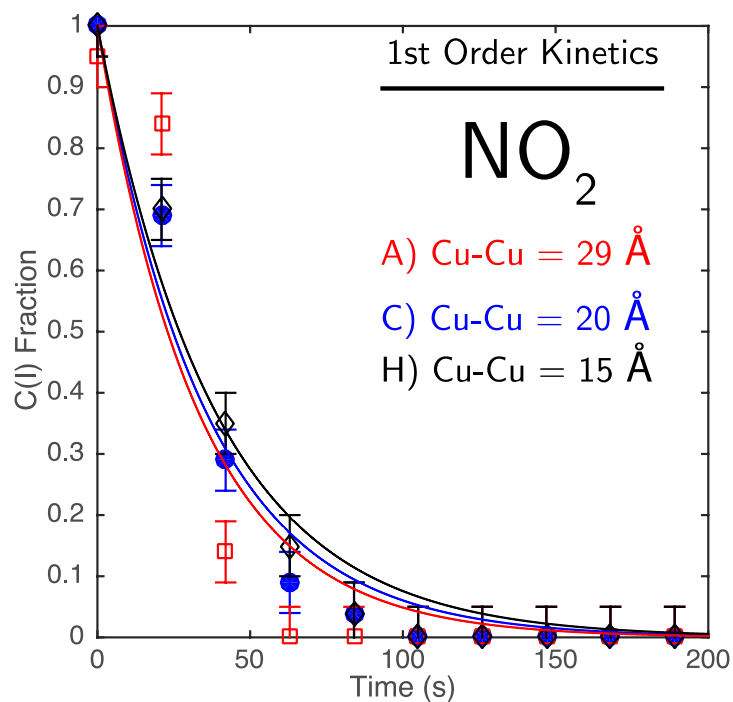


Fig. S13. Temporal evolution of the XANES-measured Cu^{I} fraction in Cu-CHA-29 (A, red), Cu-CHA-20 (C, blue), and Cu-CHA-15 (H, black) during transient oxidation in 100 ppm NO_2 at 473 K. Least-squares fit to Eq. S11 is shown by solid lines.

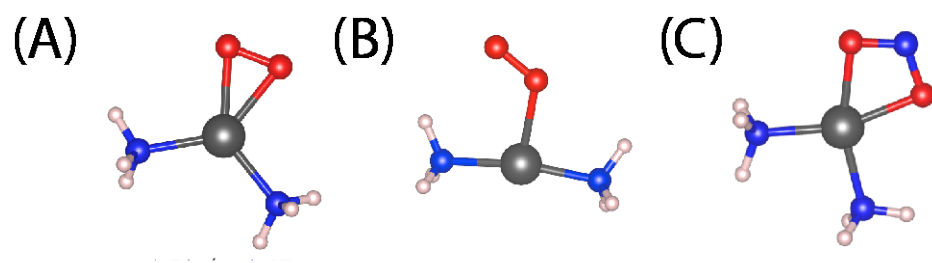


Fig. S14. Structures for O₂ configuration (A), O₂ configuration (B) and NO₂ (C) adsorbed on a single Cu^I(NH₃)₂. Calculations were performed in the CHA supercell described in S5, and the framework removed from this figure for clarity.

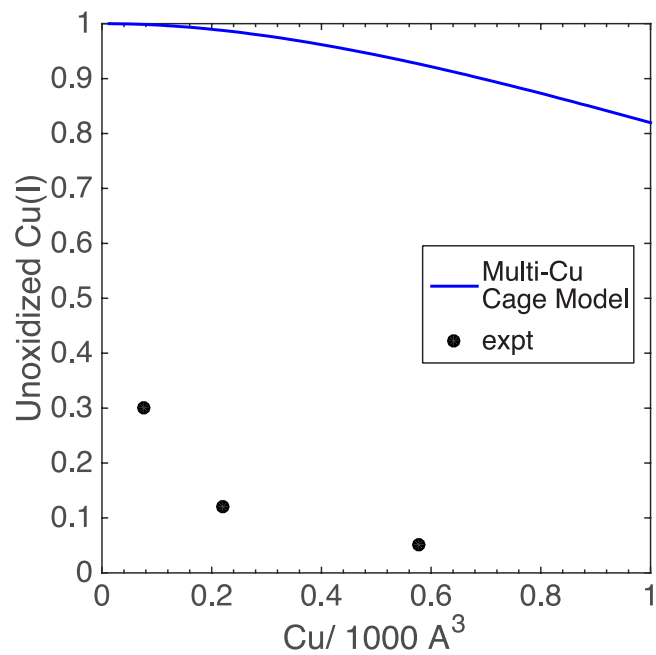


Fig. S15. The fraction of lone Cu within zeolite cages randomly dispersed on the zeolite framework unable to oxidize compared with experimental measurements.

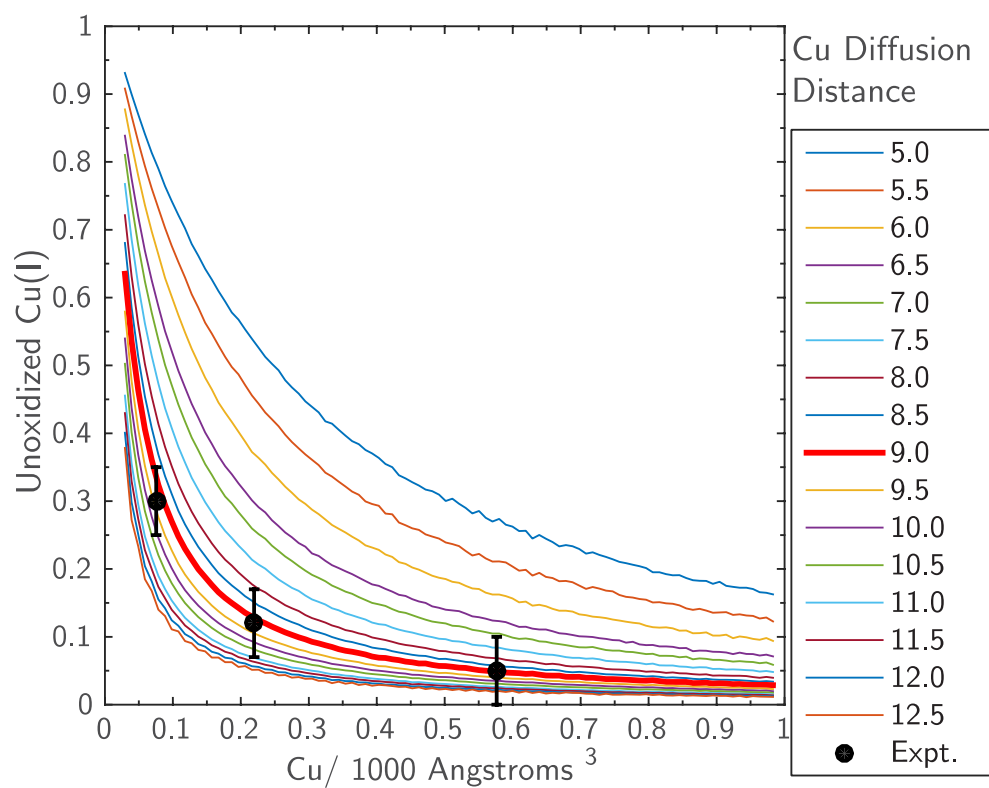


Fig. S16. Fraction of unoxidizable Cu^I as a function of Cu density from simulation. Splines were drawn through the discrete simulations at each density to yield continuous curves in the figure. 9 Å (bold red line) represents the metadynamics-predicted maximum Cu diffusion distance. Black data points are experimental observations from Figure 3A.

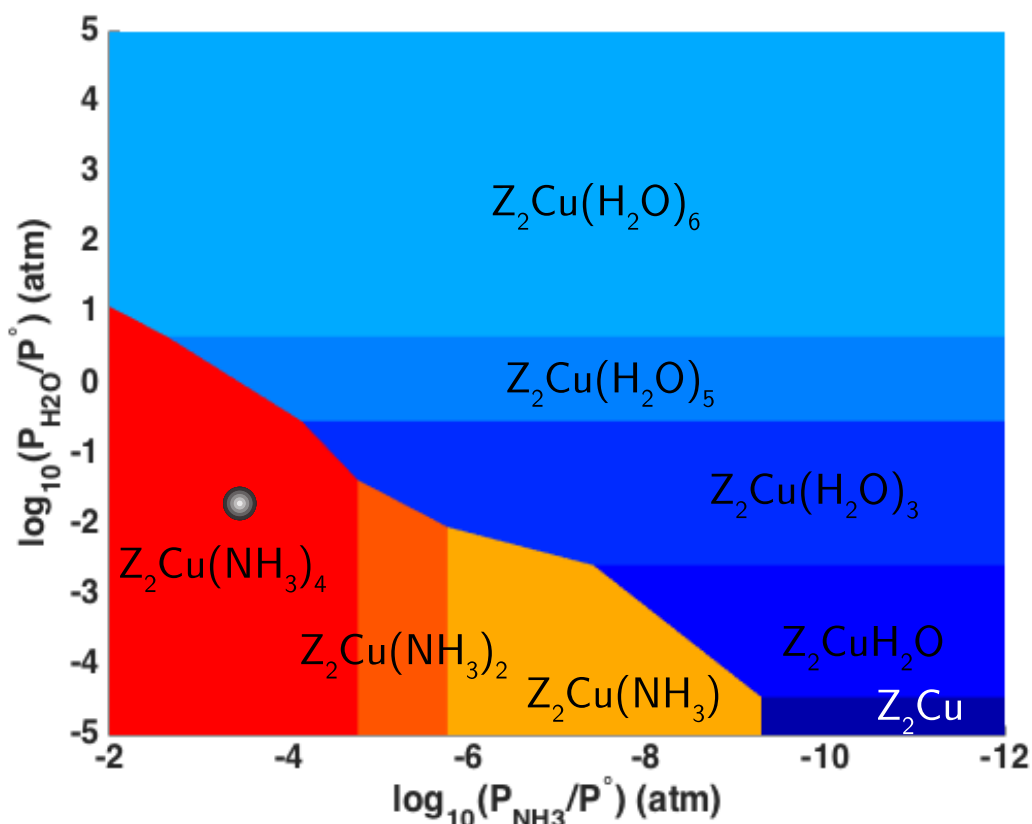


Fig. S17. Phase diagrams for 2Al (“Z₂”) exchanged Cu sites with varying P_{NH₃} and P_{H₂O} at 473 K and 10% O₂. The chrome sphere demarcates NH₃ and H₂O pressures equivalent to those used in the kinetic experiments reported in figure 1B and figure 2. All DFT-computed structures, energies, and methods used to generate this diagram can be found in Paolucci et al. (10).

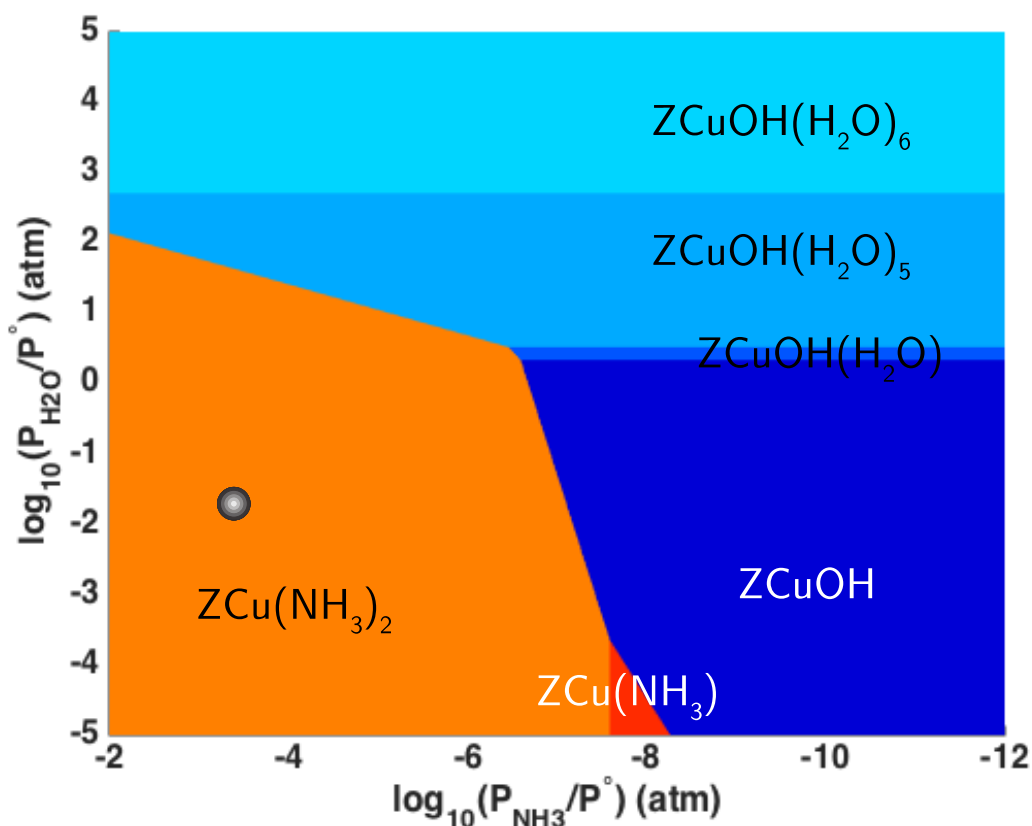


Fig. S18. Phase diagrams for 1Al (“Z”) exchanged Cu sites with varying P_{NH_3} and $P_{\text{H}_2\text{O}}$ at 473 K and 10% O_2 . The chrome sphere demarcates NH_3 and H_2O pressures equivalent to those used in the kinetic experiments reported in figure 1B and figure 2. All DFT-computed structures, energies, and methods used to generate this diagram can be found in Paolucci et al. (10).

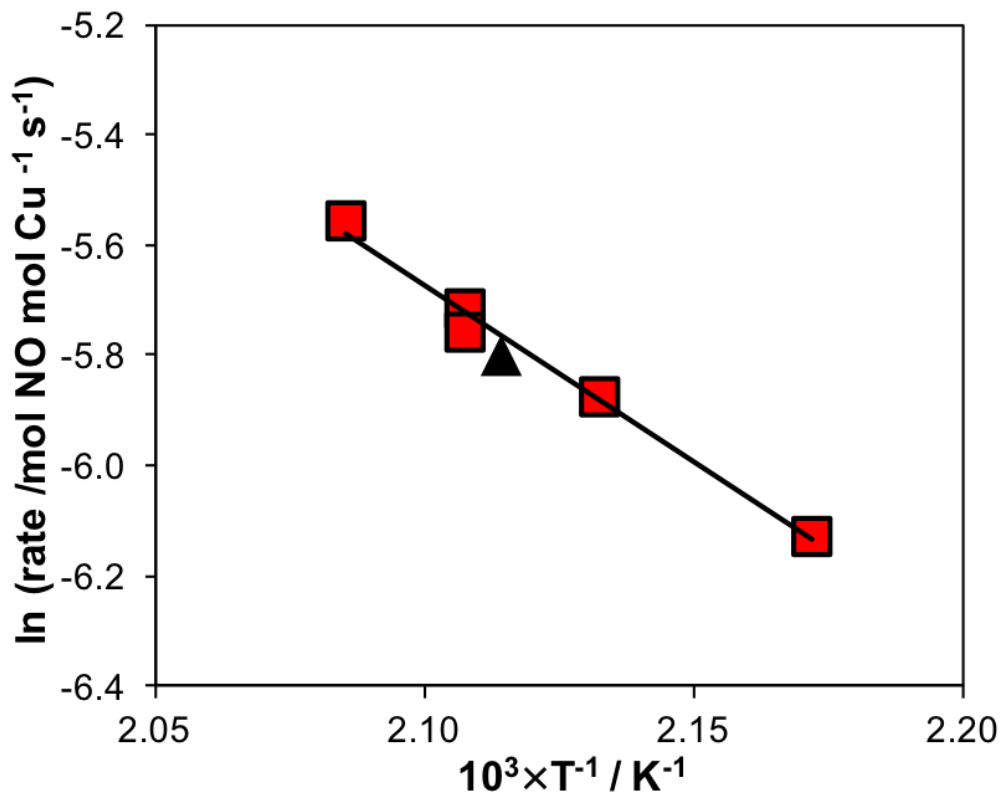


Fig. S20. Standard SCR rates (300 ppm NO, 300 ppm NH₃, 10% O₂, 7% CO₂, 3% H₂O and balance N₂) measured in the temperature range of 450-480 K on Cu-CHA-19 in the laboratory differential PFR (red squares) and in the *operando* XAS reactor (black triangle). Line denotes regression of an Arrhenius rate equation to the lab PFR rate data.

Table S1. Bulk elemental analysis and fraction of isolated Cu^{II} and Cu^{II}(OH) sites on a series of Cu-exchanged SSZ-13 samples with varying Si/Al (4.5-25) and Cu/Al (0.03-0.59); arranged by increasing Cu/Al for a fixed Si/Al ratio.

Si/Al	Cu/Al	Cu wt%	H ⁺ /Al (H-form)	H ⁺ /Al (Cu-form)	Cu ^{II} OH/Al*	Cu ^{II} /Al*
4.5	0.08	1.4	0.46	0.31	0	0.08
4.5	0.21	3.7	0.87	0.42	0	0.21
15	0.03	0.3	0.98	0.93	0	0.03
15	0.08	0.5	0.98	0.81	0	0.08
15	0.10	0.7	0.98	0.80	0.01	0.09
15	0.12	0.8	0.98	0.73	0.03	0.09
15	0.19	1.3	0.98	0.68	0.10	0.09
15	0.25	1.7	1.00	0.64	0.16	0.09
15	0.37	2.4	0.98	0.58	0.28	0.09
15	0.44	2.9	0.98	0.51	0.35	0.09
25	0.21	0.8	0.98	0.74	0.17	0.04
25	0.42	1.6	0.98	0.58	0.37	0.04
25	0.59	2.4	0.98	0.47	0.55	0.04

*Determined from titration of residual H⁺ sites by NH₃ and thermodynamic preferences for Cu^{II} and Cu^{II}OH siting (10).

Table S2. A series of Cu-exchanged SSZ-13 samples with varying Si/Al (4.5-25) and Cu/Al (0.03-0.44) (X = Mean Cu-Cu distance in Å, rounded down, labels (a-h) correspond to those in Figure 2); arranged by increasing Cu/Al for a fixed Si/Al ratio.

Si/Al	Cu/Al	Cu cation density (mol Cu/m ³)	Cu /1000Å ³	Cu per CHA cage	Mean Cu-Cu distance (Å)	Cu-CHA-X
4.5	0.08	365	0.22	0.17	20.6	Cu-CHA-20 (c)
4.5	0.21	958	0.57	0.44	15.0	Cu-CHA-15 (h)
15	0.03	47	0.03	0.02	40.7	Cu-CHA-40
15	0.08	125	0.07	0.05	29.4	Cu-CHA-29 (a)
15	0.10	157	0.09	0.07	27.2	Cu-CHA-27
15	0.12	188	0.11	0.08	25.6	Cu-CHA-25
15	0.19	298	0.18	0.14	22.0	Cu-CHA-22
15	0.25	395	0.23	0.18	20.1	Cu-CHA-20*
15	0.37	580	0.35	0.27	17.6	Cu-CHA-17 (f)
15	0.44	689	0.41	0.31	16.6	Cu-CHA-16 (g)
25	0.21	193	0.11	0.08	25.4	Cu-CHA-25 (b)
25	0.42	395	0.24	0.18	19.8	Cu-CHA-19 (d)
25	0.59	569	0.34	0.26	17.7	Cu-CHA-17*(e)

*Identifies the higher Si/Al density sample of two samples that share the same mean (rounded down) Cu-Cu distance.

Table S3. Standard SCR kinetic parameters measured on a series of Cu-exchanged SSZ-13 samples with Si/Al = 15 and Cu/Al varying from 0.03-0.44; arranged by increasing Cu/Al. (X = Mean Cu-Cu distance in Å, rounded down, labels (a, f, and g) correspond to those in Figure 2)

Cu-CHA-X	Cu /1000Å ³	SCR Rate (/10 ⁻³ mol NO/mol Cu/s)	SCR Rate (/10 ⁻³ NO/1000Å ³ /s)	O ₂ order [†]	E _{app} [‡] (kJ mol ⁻¹)
Cu-CHA-40 (a)	0.03	1.8	0.05	0.8	47
Cu-CHA-29	0.07	2.3	0.16	0.7	50
Cu-CHA-27	0.09	3.3	0.30	0.7	56
Cu-CHA-25	0.11	4.5	0.50	0.7	56
Cu-CHA-22	0.18	6.5	1.17	0.5	60
Cu-CHA-20*	0.23	7.8	1.79	0.4	63
Cu-CHA-17 (f)	0.35	7.4	2.59	0.4	66
Cu-CHA-16 (g)	0.41	7.8	3.20	0.3	74

*Identifies the higher Si/Al density sample of two samples that share the same mean (rounded down) Cu-Cu distance.

†Errors in the apparent O₂ rate order are ± 0.1.

‡Errors in the apparent activation energy (E_{app}) are ± 7 kJ/mol. Consistent with prior reports (17, 18) E_{app} increases systematically with increasing Cu density, reflecting the gradual transition from a kinetic regime in which O₂ activation is rate-determining (low Cu density) to one in which it is not (high Cu density).

Table S4. *Operando* steady state Cu^I fraction for a series of Cu-SSZ-13 samples with varying Cu density from 0.07-0.57 atom/1000Å³. Feed conditions: 300 ppm NO, 300 ppm NH₃, 10% O₂, 5% CO₂, 2% H₂O, 473 K.

Si/Al	Cu/Al	Cu-CHA-X	Cu cation density (Cu/1000Å ³)	<i>Operando</i> steady state Cu ^I fraction [†]	EXAFS first shell coordination number
4.5	0.08	Cu-CHA-20 (c)	0.22	0.50	3.4
4.5	0.21	Cu-CHA-15 (h)	0.57	0.10	3.9
15	0.08	Cu-CHA-29 (a)	0.07	0.96	2.1
15	0.37	Cu-CHA-17 (f)	0.35	0.53	3.2
15	0.44	Cu-CHA-16 (g)	0.41	0.47	3.3
25	0.21	Cu-CHA-25 (b)	0.11	0.85	2.4
25	0.42	Cu-CHA-19 (d)	0.24	0.63	2.8
25	0.59	Cu-CHA-17*(e)	0.34	0.51	3.1
16 (19)	0.20	-	0.18	0.60	-
4.5 (17)	0.16	-	0.44	0.26	-

*Identifies the higher Si/Al density sample of two samples that share the same mean (rounded down) Cu-Cu distance.

[†]Errors are ± 0.05.

Table S5. Comparison of standard SCR reaction rates measured in the PFR and the *operando* reactor for different Cu-CHA samples. Feed conditions: 300 ppm NO, 300 ppm NH₃, 10% O₂, 5% CO₂, 2% H₂O, 473 K.

Si/Al	Cu/Al	Cu-CHA-X	PFR Rate (/10 ⁻³ mol NO/mol Cu/s)	<i>Operando</i> Reactor Rate (/10 ⁻³ mol NO/mol Cu/s)
4.5	0.08	Cu-CHA-20	8.3	8.0
4.5	0.21	Cu-CHA-15	7.4	7.5
15	0.08	Cu-CHA-29	2.3	2.0
15	0.37	Cu-CHA-17	7.4	7.4
15	0.44	Cu-CHA-16	7.8	7.7
25	0.21	Cu-CHA-25	1.6	1.5
25	0.42	Cu-CHA-19	3.8	3.1
25	0.59	Cu-CHA-17*	7.7	7.0

*Identifies the higher Si/Al density sample of two samples that share the same mean (rounded down) Cu-Cu distance.

Table S6. Fitted Cu^I fraction before and after oxidation with 10% O₂ at 473 K starting from Cu^I(NH₃)₂ for Cu-CHA-20, Cu-CHA-15 and Cu-CHA-29.

Cu-CHA-X	Cu^I fraction before O₂ transients *	Cu^I fraction after O₂ transients *
Cu-CHA-20	0.90	0.12
Cu-CHA-15	0.90	0.05
Cu-CHA-29	0.98	0.30

*Fitting error ± 0.05.

Table S7. Fitted Cu^I fraction before and after repeated subsequent oxidation with 10% O₂ at 473 K starting from Cu^I(NH₃)₂ in each cycle for Cu-CHA-29.

Cu^I fraction before O₂ transients	Cu^I fraction after O₂ transients
Cycle 1	
0.98	0.30
Cycle 2	
0.95	0.32
Cycle 3	
0.98	0.31

Table S8. Fitted Cu^I fraction before and after oxidation with 100 ppm NO₂ at 473 K starting from Cu^I(NH₃)₂ for Cu-CHA-20, Cu-CHA-15 and Cu-CHA-29.

Cu-CHA-X	Cu^I fraction before NO₂ transients	Cu^I fraction after NO₂ transients
Cu-CHA-20	0.90	0.00
Cu-CHA-15	0.90	0.00
Cu-CHA-29	0.98	0.00

Table S9. PBE+D2 DFT computed reaction energies (column 2), total energy differences along the reaction coordinate (column 3), and normalized Bader charge (*l*₀) derived Cu oxidation states for the product in each step (column 4) for all results reported in Figure 4.

Reaction	Reaction Energy		Cu Oxidation State
	(kJ mol ⁻¹)	Energy (kJ mol ⁻¹)	
A	-	0	1.00
A → TS1	35	35	
TS1 → B	23	23	1.00
B → C	-59	-36	1.39
C → TS2	20, Ref (24)	-16	
TS2 → D	-26	-42	1.80
D → TS3	19	-23	
TS3 → E	-36	-60	2.10

Table S10. Computed PBE+D2 and HSE06+TSvdw reaction energies for O₂ and NO₂ adsorption on a Cu^I(NH₃)₂ monomer. Rows 1 and 2 reference the two different (A, B) O₂ adsorption configurations in Figure S14. Columns 3 and 5 report the normalized Bader charge (*l*₀) derived Cu oxidation state.

	PBE+D2 (kJ mol⁻¹)	Cu Oxidation State	HSE06+TSvdw (kJ mol⁻¹)	Cu Oxidation State
Cu ^I (NH ₃) ₂ +O ₂ (A)	2	1.65	1	1.47
Cu ^I (NH ₃) ₂ +O ₂ (B)	-26	1.32	-11	1.15
Cu ^I (NH ₃) ₂ +NO ₂ (C)	-46	1.92	-71	2.27

Table S11. Metadynamics parameters.

Parameter	CV
Harmonic spring constant, k (hartree)	5
Mass of the fictitious particle, μ (hartree (a.u.) ²)	100
Gaussian height, W (hartree)	0.0005
Gaussian width, s'	0.02
Minimum Metadynamics time step, Δt_{\min} (a.u.)	100
p	6
q	6
d_0 (Å)	6.2

References and Notes

1. J. M. Thomas, The societal significance of catalysis and the growing practical importance of single-site heterogeneous catalysts. *Proc. R. Soc. A* **468**, 1884–1903 (2012). [doi:10.1098/rspa.2012.0196](https://doi.org/10.1098/rspa.2012.0196)
2. M. Boudart, Turnover rates in heterogeneous catalysis. *Chem. Rev.* **95**, 661–666 (1995). [doi:10.1021/cr00035a009](https://doi.org/10.1021/cr00035a009)
3. K. Ding, A. Gulec, A. M. Johnson, N. M. Schweitzer, G. D. Stucky, L. D. Marks, P. C. Stair, Identification of active sites in CO oxidation and water-gas shift over supported Pt catalysts. *Science* **350**, 189–192 (2015). [doi:10.1126/science.aac6368](https://doi.org/10.1126/science.aac6368) [Medline](#)
4. J. Jones, H. Xiong, A. T. DeLaRiva, E. J. Peterson, H. Pham, S. R. Challa, G. Qi, S. Oh, M. H. Wiebenga, X. I. Pereira Hernández, Y. Wang, A. K. Datye, Thermally stable single-atom platinum-on-ceria catalysts via atom trapping. *Science* **353**, 150–154 (2016). [doi:10.1126/science.aaf8800](https://doi.org/10.1126/science.aaf8800) [Medline](#)
5. E. J. Peterson, A. T. DeLaRiva, S. Lin, R. S. Johnson, H. Guo, J. T. Miller, J. Hun Kwak, C. H. F. Peden, B. Kiefer, L. F. Allard, F. H. Ribeiro, A. K. Datye, Low-temperature carbon monoxide oxidation catalysed by regenerable atomically dispersed palladium on alumina. *Nat. Commun.* **5**, 4885 (2014). [doi:10.1038/ncomms5885](https://doi.org/10.1038/ncomms5885) [Medline](#)
6. G. Kyriakou, M. B. Boucher, A. D. Jewell, E. A. Lewis, T. J. Lawton, A. E. Baber, H. L. Tierney, M. Flytzani-Stephanopoulos, E. C. H. Sykes, Isolated metal atom geometries as a strategy for selective heterogeneous hydrogenations. *Science* **335**, 1209–1212 (2012). [doi:10.1126/science.1215864](https://doi.org/10.1126/science.1215864) [Medline](#)
7. H. Wei, X. Liu, A. Wang, L. Zhang, B. Qiao, X. Yang, Y. Huang, S. Miao, J. Liu, T. Zhang, FeO_x-supported platinum single-atom and pseudo-single-atom catalysts for chemoselective hydrogenation of functionalized nitroarenes. *Nat. Commun.* **5**, 5634 (2014). [doi:10.1038/ncomms6634](https://doi.org/10.1038/ncomms6634) [Medline](#)
8. M. Yang, S. Li, Y. Wang, J. A. Herron, Y. Xu, L. F. Allard, S. Lee, J. Huang, M. Mavrikakis, M. Flytzani-Stephanopoulos, Catalytically active Au-O(OH)_x-species stabilized by alkali ions on zeolites and mesoporous oxides. *Science* **346**, 1498–1501 (2014). [doi:10.1126/science.1260526](https://doi.org/10.1126/science.1260526) [Medline](#)
9. M. Yang, J. Liu, S. Lee, B. Zugic, J. Huang, L. F. Allard, M. Flytzani-Stephanopoulos, A common single-site Pt(II)-O(OH)_x-species stabilized by sodium on “active” and “inert” supports catalyzes the water-gas shift reaction. *J. Am. Chem. Soc.* **137**, 3470–3473 (2015). [doi:10.1021/ja513292k](https://doi.org/10.1021/ja513292k) [Medline](#)
10. C. Paolucci, A. A. Parekh, I. Khurana, J. R. Di Iorio, H. Li, J. D. Albarracin Caballero, A. J. Shih, T. Anggara, W. N. Delgass, J. T. Miller, F. H. Ribeiro, R. Gounder, W. F. Schneider, Catalysis in a cage: Condition-dependent speciation and dynamics of exchanged Cu cations in SSZ-13 zeolites. *J. Am. Chem. Soc.* **138**, 6028–6048 (2016). [doi:10.1021/jacs.6b02651](https://doi.org/10.1021/jacs.6b02651) [Medline](#)
11. J. M. Thomas, R. Raja, D. W. Lewis, Single-site heterogeneous catalysts. *Angew. Chem. Int. Ed.* **44**, 6456–6482 (2005). [doi:10.1002/anie.200462473](https://doi.org/10.1002/anie.200462473) [Medline](#)

12. C. Paolucci, J. Di Iorio, F. Ribeiro, R. Gounder, W. Schneider, "Catalysis science of NO_x selective catalytic reduction with ammonia over Cu-SSZ-13 and Cu-SAPO-34," in *Advances in Catalysis*, C. Song, Ed. (Elsevier, 2016), vol. 59, pp. 1–107.
13. S. T. Korhonen, D. W. Fickel, R. F. Lobo, B. M. Weckhuysen, A. M. Beale, Isolated Cu²⁺ ions: Active sites for selective catalytic reduction of NO. *Chem. Commun. (Camb.)* **47**, 800–802 (2011). [doi:10.1039/C0CC04218H](https://doi.org/10.1039/C0CC04218H) [Medline](#)
14. E. Borfecchia, K. A. Lomachenko, F. Giordanino, H. Falsig, P. Beato, A. V. Soldatov, S. Bordiga, C. Lamberti, Revisiting the nature of Cu sites in the activated Cu-SSZ-13 catalyst for SCR reaction. *Chem. Sci. (Camb.)* **6**, 548–563 (2015). [doi:10.1039/C4SC02907K](https://doi.org/10.1039/C4SC02907K)
15. C. Paolucci, A. A. Verma, S. A. Bates, V. F. Kispersky, J. T. Miller, R. Gounder, W. N. Delgass, F. H. Ribeiro, W. F. Schneider, Isolation of the copper redox steps in the standard selective catalytic reduction on Cu-SSZ-13. *Angew. Chem. Int. Ed.* **53**, 11828–11833 (2014). [doi:10.1002/anie.201407030](https://doi.org/10.1002/anie.201407030) [Medline](#)
16. T. V. W. Janssens, H. Falsig, L. F. Lundegaard, P. N. R. Vennestrom, S. B. Rasmussen, P. G. Moses, F. Giordanino, E. Borfecchia, K. A. Lomachenko, C. Lamberti, S. Bordiga, A. Godiksen, S. Mossin, P. Beato, A consistent reaction scheme for the selective catalytic reduction of nitrogen oxides with ammonia. *ACS Catal.* **5**, 2832–2845 (2015). [doi:10.1021/cs501673g](https://doi.org/10.1021/cs501673g)
17. S. A. Bates, A. A. Verma, C. Paolucci, A. A. Parekh, T. Anggara, A. Yezerets, W. F. Schneider, J. T. Miller, W. N. Delgass, F. H. Ribeiro, Identification of the active Cu site in standard selective catalytic reduction with ammonia on Cu-SSZ-13. *J. Catal.* **312**, 87–97 (2014). [doi:10.1016/j.jcat.2014.01.004](https://doi.org/10.1016/j.jcat.2014.01.004)
18. F. Gao, E. D. Walter, M. Kollar, Y. Wang, J. Szanyi, C. H. F. Peden, Understanding ammonia selective catalytic reduction kinetics over Cu/SSZ-13 from motion of the Cu ions. *J. Catal.* **319**, 1–14 (2014). [doi:10.1016/j.jcat.2014.08.010](https://doi.org/10.1016/j.jcat.2014.08.010)
19. T. Günter, H. W. P. Carvalho, D. E. Doronkin, T. Sheppard, P. Glatzel, A. J. Atkins, J. Rudolph, C. R. Jacob, M. Casapu, J.-D. Grunwaldt, Structural snapshots of the SCR reaction mechanism on Cu-SSZ-13. *Chem. Commun. (Camb.)* **51**, 9227–9230 (2015). [doi:10.1039/C5CC01758K](https://doi.org/10.1039/C5CC01758K) [Medline](#)
20. K. A. Lomachenko, E. Borfecchia, C. Negri, G. Berlier, C. Lamberti, P. Beato, H. Falsig, S. Bordiga, The Cu-CHA deNO_x catalyst in action: Temperature-dependent NH₃-assisted selective catalytic reduction monitored by operando XAS and XES. *J. Am. Chem. Soc.* **138**, 12025–12028 (2016). [doi:10.1021/jacs.6b06809](https://doi.org/10.1021/jacs.6b06809) [Medline](#)
21. P. J. Smeets, R. G. Hadt, J. S. Woertink, P. Vanelderen, R. A. Schoonheydt, B. F. Sels, E. I. Solomon, Oxygen precursor to the reactive intermediate in methanol synthesis by Cu-ZSM-5. *J. Am. Chem. Soc.* **132**, 14736–14738 (2010). [doi:10.1021/ja106283u](https://doi.org/10.1021/ja106283u) [Medline](#)
22. P. Vanelderen, B. E. R. Snyder, M.-L. Tsai, R. G. Hadt, J. Vancauwenbergh, O. Coussens, R. A. Schoonheydt, B. F. Sels, E. I. Solomon, Spectroscopic definition of the copper active sites in mordenite: Selective methane oxidation. *J. Am. Chem. Soc.* **137**, 6383–6392 (2015). [doi:10.1021/jacs.5b02817](https://doi.org/10.1021/jacs.5b02817) [Medline](#)

23. J. S. Woertink, P. J. Smeets, M. H. Groothaert, M. A. Vance, B. F. Sels, R. A. Schoonheydt, E. I. Solomon, A $[\text{Cu}_2\text{O}]^{2+}$ core in Cu-ZSM-5, the active site in the oxidation of methane to methanol. *Proc. Natl. Acad. Sci. U.S.A.* **106**, 18908–18913 (2009). [doi:10.1073/pnas.0910461106](https://doi.org/10.1073/pnas.0910461106) [Medline](#)
24. M. Metz, E. I. Solomon, Dioxygen binding to deoxyhemocyanin: Electronic structure and mechanism of the spin-forbidden two-electron reduction of O_2 . *J. Am. Chem. Soc.* **123**, 4938–4950 (2001). [doi:10.1021/ja004166b](https://doi.org/10.1021/ja004166b) [Medline](#)
25. L. M. Mirica, X. Ottenwaelder, T. D. P. Stack, Structure and spectroscopy of copper-dioxygen complexes. *Chem. Rev.* **104**, 1013–1045 (2004). [doi:10.1021/cr020632z](https://doi.org/10.1021/cr020632z) [Medline](#)
26. L. M. Mirica, M. Vance, D. J. Rudd, B. Hedman, K. O. Hodgson, E. I. Solomon, T. D. Stack, Tyrosinase reactivity in a model complex: An alternative hydroxylation mechanism. *Science* **308**, 1890–1892 (2005). [doi:10.1126/science.1112081](https://doi.org/10.1126/science.1112081) [Medline](#)
27. P. Chen, E. I. Solomon, O_2 activation by binuclear Cu sites: Noncoupled versus exchange coupled reaction mechanisms. *Proc. Natl. Acad. Sci. U.S.A.* **101**, 13105–13110 (2004). [doi:10.1073/pnas.0402114101](https://doi.org/10.1073/pnas.0402114101) [Medline](#)
28. S. D. McCann, S. S. Stahl, Copper-catalyzed aerobic oxidations of organic molecules: Pathways for two-electron oxidation with a four-electron oxidant and a one-electron redox-active catalyst. *Acc. Chem. Res.* **48**, 1756–1766 (2015). [doi:10.1021/acs.accounts.5b00060](https://doi.org/10.1021/acs.accounts.5b00060) [Medline](#)
29. B. R. Goodman, K. C. Hass, W. F. Schneider, J. B. Adams, Cluster model studies of oxygen-bridged Cu pairs in Cu-ZSM-5 catalysts. *J. Phys. Chem. B* **103**, 10452–10460 (1999). [doi:10.1021/jp9922110](https://doi.org/10.1021/jp9922110)
30. E. I. Solomon, D. E. Heppner, E. M. Johnston, J. W. Ginsbach, J. Cirera, M. Qayyum, M. T. Kieber-Emmons, C. H. Kjaergaard, R. G. Hadt, L. Tian, Copper active sites in biology. *Chem. Rev.* **114**, 3659–3853 (2014). [doi:10.1021/cr400327t](https://doi.org/10.1021/cr400327t) [Medline](#)
31. L. Chen, J. Jansson, M. Skoglundh, H. Grönbeck, Mechanism for solid-state ion exchange of Cu^+ into zeolites. *J. Phys. Chem. C* **120**, 29182–29189 (2016). [doi:10.1021/acs.jpcc.6b09553](https://doi.org/10.1021/acs.jpcc.6b09553)
32. H. Falsig, P. N. R. Vennestrøm, P. G. Moses, T. V. W. Janssens, Activation of oxygen and NO in NH_3 -SCR over Cu-CHA catalysts evaluated by density functional theory. *Top. Catal.* **59**, 861–865 (2016). [doi:10.1007/s11244-016-0560-8](https://doi.org/10.1007/s11244-016-0560-8)
33. W. Lowenstein, The distribution of aluminium in the tetrahedra of silicates and aluminates. *Am. Mineral.* **39**, 92–96 (1954).
34. F. Gao, D. Mei, Y. Wang, J. Szanyi, C. H. F. Peden, Selective catalytic reduction over Cu/SSZ-13: Linking homo- and heterogeneous catalysis. *J. Am. Chem. Soc.* **139**, 4935–4942 (2017). [doi:10.1021/jacs.7b01128](https://doi.org/10.1021/jacs.7b01128) [Medline](#)
35. J. H. Kwak, R. G. Tonkyn, D. H. Kim, J. Szanyi, C. H. F. Peden, Excellent activity and selectivity of Cu-SSZ-13 in the selective catalytic reduction of NO_x with NH_3 . *J. Catal.* **275**, 187–190 (2010). [doi:10.1016/j.jcat.2010.07.031](https://doi.org/10.1016/j.jcat.2010.07.031)

36. C. Baerlocher, L. B. McCusker, Database of zeolite structures (2017); www.iza-structure.org/databases/.
37. G. Lambel, A. Moen, D. G. Nicholson, Structure of the diamminecopper(I) ion in solution. An X-ray absorption spectroscopic study. *J. Chem. Soc. Faraday Trans.* **90**, 2211–2213 (1994). [doi:10.1039/ft9949002211](https://doi.org/10.1039/ft9949002211)
38. L.-S. Kau, D. J. Spira-Solomon, J. E. Penner-Hahn, K. O. Hodgson, E. I. Solomon, X-ray absorption edge determination of the oxidation state and coordination number of copper: Application to the type 3 site in *Rhus vernicifera* laccase and its reaction with oxygen. *J. Am. Chem. Soc.* **109**, 6433–6442 (1987). [doi:10.1021/ja00255a032](https://doi.org/10.1021/ja00255a032)
39. V. F. Kispersky, A. J. Kropf, F. H. Ribeiro, J. T. Miller, Low absorption vitreous carbon reactors for operando XAS: A case study on Cu/Zeolites for selective catalytic reduction of NO_x by NH₃. *Phys. Chem. Chem. Phys.* **14**, 2229–2238 (2012). [doi:10.1039/C1CP22992C](https://doi.org/10.1039/C1CP22992C) [Medline](#)
40. A. A. Verma, S. A. Bates, T. Anggara, C. Paolucci, A. A. Parekh, K. Kamasamudram, A. Yezerets, J. T. Miller, W. N. Delgass, W. F. Schneider, F. H. Ribeiro, NO oxidation: A probe reaction on Cu-SSZ-13. *J. Catal.* **312**, 179–190 (2014). [doi:10.1016/j.jcat.2014.01.017](https://doi.org/10.1016/j.jcat.2014.01.017)
41. M. H. Groothaert, K. Lievens, J. A. van Bokhoven, A. A. Battiston, B. M. Weckhuysen, K. Pierloot, R. A. Schoonheydt, Bis(μ-oxo)dicopper as key intermediate in the catalytic decomposition of nitric oxide. *ChemPhysChem* **4**, 626–630 (2003). [doi:10.1002/cphc.200300746](https://doi.org/10.1002/cphc.200300746) [Medline](#)
42. J. R. Di Iorio, S. A. Bates, A. A. Verma, W. N. Delgass, F. H. Ribeiro, J. T. Miller, R. Gounder, The dynamic nature of Brønsted acid sites in Cu–Zeolites during NO_x selective catalytic reduction: Quantification by gas-phase ammonia titration. *Top. Catal.* **58**, 424–434 (2015). [doi:10.1007/s11244-015-0387-8](https://doi.org/10.1007/s11244-015-0387-8)
43. S. Bordiga, E. Groppo, G. Agostini, J. A. van Bokhoven, C. Lamberti, Reactivity of surface species in heterogeneous catalysts probed by in situ X-ray absorption techniques. *Chem. Rev.* **113**, 1736–1850 (2013). [doi:10.1021/cr2000898](https://doi.org/10.1021/cr2000898) [Medline](#)
44. J. A. Van Bokhoven, C. Lamberti, *X-ray Absorption and X-ray Emission Spectroscopy: Theory and Applications* (Wiley, 2016), vol. 1.
45. C. Lamberti, S. Bordiga, F. Bonino, C. Prestipino, G. Berlier, L. Capello, F. D’Acapito, F. X. Llabrés i Xamena, A. Zecchina, Determination of the oxidation and coordination state of copper on different Cu-based catalysts by XANES spectroscopy in situ or in operando conditions. *Phys. Chem. Chem. Phys.* **5**, 4502–4509 (2003). [doi:10.1039/B305810G](https://doi.org/10.1039/B305810G)
46. F. Giordanino, P. N. R. Vennestrøm, L. F. Lundegaard, F. N. Stappen, S. Mossin, P. Beato, S. Bordiga, C. Lamberti, Characterization of Cu-exchanged SSZ-13: A comparative FTIR, UV-Vis, and EPR study with Cu-ZSM-5 and Cu-β with similar Si/Al and Cu/Al ratios. *Dalton Trans.* **42**, 12741–12761 (2013). [doi:10.1039/c3dt50732g](https://doi.org/10.1039/c3dt50732g) [Medline](#)
47. G. R. Shulman, Y. Yafet, P. Eisenberger, W. E. Blumberg, Observations and interpretation of x-ray absorption edges in iron compounds and proteins. *Proc. Natl. Acad. Sci. U.S.A.* **73**, 1384–1388 (1976). [doi:10.1073/pnas.73.5.1384](https://doi.org/10.1073/pnas.73.5.1384) [Medline](#)

48. J. E. Hahn, R. A. Scott, K. O. Hodgson, S. Doniach, S. R. Desjardins, E. I. Solomon, Observation of an electric quadrupole transition in the X-ray absorption spectrum of a Cu(II) complex. *Chem. Phys. Lett.* **88**, 595–598 (1982). [doi:10.1016/0009-2614\(82\)85016-1](https://doi.org/10.1016/0009-2614(82)85016-1)
49. F. Giordanino, E. Borfecchia, K. A. Lomachenko, A. Lazzarini, G. Agostini, E. Gallo, A. V. Soldatov, P. Beato, S. Bordiga, C. Lamberti, Interaction of NH₃ with Cu-SSZ-13 catalyst: A complementary FTIR, XANES, and XES study. *J. Phys. Chem. Lett.* **5**, 1552–1559 (2014). [doi:10.1021/jz500241m](https://doi.org/10.1021/jz500241m) [Medline](#)
50. P. N. Vennestrøm, T. V. W. Janssens, A. Kustov, M. Grill, A. Puig-Molina, L. F. Lundegaard, R. R. Tiruvalam, P. Concepción, A. Corma, Influence of lattice stability on hydrothermal deactivation of Cu-ZSM-5 and Cu-IM-5 zeolites for selective catalytic reduction of NO_x by NH₃. *J. Catal.* **309**, 477–490 (2014). [doi:10.1016/j.jcat.2013.10.017](https://doi.org/10.1016/j.jcat.2013.10.017)
51. D.-J. Liu, H. J. Robota, On the mechanism of NO selective catalytic reduction by hydrocarbons over Cu-ZSM-5 via X-ray absorption spectroscopic study. *J. Phys. Chem. B* **103**, 2755–2765 (1999). [doi:10.1021/jp9837611](https://doi.org/10.1021/jp9837611)
52. D.-J. Liu, H. J. Robota, In situ XANES characterization of the Cu oxidation state in Cu-ZSM-5 during NO decomposition catalysis. *Catal. Lett.* **21**, 291–301 (1993). [doi:10.1007/BF00769481](https://doi.org/10.1007/BF00769481)
53. Y. Kuroda, Y. Yoshikawa, S. Konno, H. Hamano, H. Maeda, R. Kumashiro, M. Nagao, Specific feature of copper ion-exchanged mordenite for dinitrogen adsorption at room-temperature. *J. Phys. Chem.* **99**, 10621–10628 (1995). [doi:10.1021/j100026a028](https://doi.org/10.1021/j100026a028)
54. C. Lamberti, G. Spoto, D. Scarano, C. Pazé, M. Salvalaggio, S. Bordiga, A. Zecchina, G. Turnes Palomino, F. D'Acapito, Cu I-Y and Cu II-Y zeolites: A XANES, EXAFS and visible-NIR study. *Chem. Phys. Lett.* **269**, 500–508 (1997). [doi:10.1016/S0009-2614\(97\)00297-2](https://doi.org/10.1016/S0009-2614(97)00297-2)
55. K. Mathisen, M. Stockenhuber, D. G. Nicholson, In situ XAS and IR studies on Cu:SAPO-5 and Cu:SAPO-11: the contributory role of monomeric linear copper(I) species in the selective catalytic reduction of NO_x by propene. *Phys. Chem. Chem. Phys.* **11**, 5476–5488 (2009). [doi:10.1039/b902491c](https://doi.org/10.1039/b902491c) [Medline](#)
56. A. Moen, D. G. Nicholson, M. Rønning, Studies on the pre-edge region of the X-ray absorption spectra of copper(I) oxide and the diamminocopper(I) ion. *J. Chem. Soc., Faraday Trans.* **91**, 3189–3194 (1995). [doi:10.1039/FT9959103189](https://doi.org/10.1039/FT9959103189)
57. R. Car, M. Parrinello, Unified approach for molecular dynamics and density-functional theory. *Phys. Rev. Lett.* **55**, 2471–2474 (1985). [doi:10.1103/PhysRevLett.55.2471](https://doi.org/10.1103/PhysRevLett.55.2471) [Medline](#)
58. J. P. Perdew, K. Burke, M. Ernzerhof, Generalized gradient approximation made simple. *Phys. Rev. Lett.* **77**, 3865–3868 (1996). [doi:10.1103/PhysRevLett.77.3865](https://doi.org/10.1103/PhysRevLett.77.3865) [Medline](#)
59. D. Vanderbilt, Soft self-consistent pseudopotentials in a generalized eigenvalue formalism. *Phys. Rev. B* **41**, 7892–7895 (1990). [doi:10.1103/PhysRevB.41.7892](https://doi.org/10.1103/PhysRevB.41.7892) [Medline](#)

60. G. Kresse, J. Furthmüller, Efficient iterative schemes for ab initio total-energy calculations using a plane-wave basis set. *J. Phys. Rev. B Condens. Matter* **54**, 11169–11186 (1996). [doi:10.1103/PhysRevB.54.11169](https://doi.org/10.1103/PhysRevB.54.11169) [Medline](#)
61. S. Grimme, Semiempirical GGA-type density functional constructed with a long-range dispersion correction. *J. Comput. Chem.* **27**, 1787–1799 (2006). [doi:10.1002/jcc.20495](https://doi.org/10.1002/jcc.20495) [Medline](#)
62. G. Henkelman, B. P. Uberuaga, H. Jónsson, A climbing image nudged elastic band method for finding saddle points and minimum energy paths. *J. Chem. Phys.* **113**, 9901–9904 (2000). [doi:10.1063/1.1329672](https://doi.org/10.1063/1.1329672)
63. J. Heyd, G. E. Scuseria, M. Ernzerhof, Erratum: Hybrid functionals based on a screened Coulomb potential. [*J. Chem. Phys.* **118**, 8207 (2003)] *J. Chem. Phys.* **124**, 219906 (2006). [doi:10.1063/1.2204597](https://doi.org/10.1063/1.2204597)
64. A. Tkatchenko, M. Scheffler, Accurate molecular van der Waals interactions from ground-state electron density and free-atom reference data. *Phys. Rev. Lett.* **102**, 073005 (2009). [doi:10.1103/PhysRevLett.102.073005](https://doi.org/10.1103/PhysRevLett.102.073005) [Medline](#)
65. M. Iannuzzi, A. Laio, M. Parrinello, Efficient exploration of reactive potential energy surfaces using Car-Parrinello molecular dynamics. *Phys. Rev. Lett.* **90**, 238302 (2003). [doi:10.1103/PhysRevLett.90.238302](https://doi.org/10.1103/PhysRevLett.90.238302) [Medline](#)
66. A. Barducci, M. Bonomi, M. Parrinello, Metadynamics. *Wiley Interdiscip. Rev. Comput. Mol. Sci.* **1**, 826–843 (2011). [doi:10.1002/wcms.31](https://doi.org/10.1002/wcms.31)
67. M. Rybicki, J. Sauer, Acidity of two-dimensional zeolites. *Phys. Chem. Chem. Phys.* **17**, 27873–27882 (2015). [doi:10.1039/C5CP05088J](https://doi.org/10.1039/C5CP05088J) [Medline](#)
68. J. D. Albarracin-Caballero, I. Khurana, J. R. Di Iorio, A. J. Shih, J. E. Schmidt, M. Dusselier, M. E. Davis, A. Yezerets, J. T. Miller, F. H. Ribeiro, R. Gounder, Structural and kinetic changes to small-pore Cu-zeolites after hydrothermal aging treatments and selective catalytic reduction of NO_x with ammonia. *React. Chem. Eng.* **2**, 168–179 (2017). [doi:10.1039/C6RE00198J](https://doi.org/10.1039/C6RE00198J)